Received: 25 July 2022 | Revised: 25 August 2022 | Accepted: 16 September 2022

DOI: 10.1049/rpg2.12610

IET Renewable Power Generation

The Institution of Engineering and Technology WILEY

ORIGINAL RESEARCH

Advanced control scheme and dynamic phasor modelling of grid-tied droop-controlled inverters

Ahmed Bendib[1] | **Abdelhammid Kherbachi**[2] | **Aissa Chouder**[3] | **Hafiz Ahmed**[4] | **Kamel Kara**[1]

[1]SET Laboratory, Electronics Department, Blida University, Blida, Algeria

[2]Centre de Développement des Energies Renouvelables, CDER, B.P. 62, Bouzaréah, Algiers, Algeria

[3]Electrical Engineering Laboratory (LGE), University Mohamed Boudiaf of Msila, Msila, Algeria

[4]Nuclear Futures Institute, Bangor University, Bangor, UK

Correspondence
Hafiz Ahmed, Nuclear Futures Institute, Bangor University, Bangor LL57 1 UT, UK
Email: hafiz.h.ahmed@ieee.org; hafiz.ahmed@bangor.ac.uk

Funding information
European Regional Development Fund

Abstract

This paper develops an advanced scheme, modelling, and analysis of power flow control intended for grid-connected droop-controlled VSIs within a single-phase microgrid (MG). The proposed control scheme includes a power calculation method based on an enhanced second-order generalized integrator frequency-locked loop (ESOGI-FLL). Contrary to the existing power calculation methods that use low-pass filter (LPF) with a low cutoff frequency to reject the grid voltage distortion and achieve average power, which may result in reducing the power calculation speed, the involved ESOGI-FLL can offer a fast transient response and benefits from high filtering capability of sub- and low-order harmonics. In addition, the ESOGI-FLL provides total rejection of the DC offset, which is another issue that may adversely affect the accuracy of the traditional methods. Thus, this proposal can contribute to improving the speed and accuracy of the power computation and make the power calculation scheme immune to DC disturbance, thereby enhancing the performance of the power control. On the other hand, a dynamic phasor modelling approach is adopted considering the dynamics of the ESOGI-based power calculation, instead of the LPF transfer function used to describe the power computation dynamic in the related works. The small-signal model of the grid-connected VSI power flow considering the line impedance R/X ratio as well as that describing the dynamics of the ESOGI-based power calculation are derived. Using these models, the closed-loop model of the grid-interactive inverter including the power controller dynamics is obtained. The system stability is assessed, which helps to determine properly the controller's gains. A simulation study of a grid-connected VSI is carried out in MATLAB/Simulink™ and PSIM's processor in the loop (PIL) platforms to assess the effectiveness of the proposed control approach. The results confirm the effectiveness of the proposed control to regulate real and reactive powers with good transient performances when the grid is subject to several working conditions.

1 | INTRODUCTION

Nowadays, microgrids (MGs) paradigm is seen as an interesting concept and an effective way of integrating renewable energy sources within a wide distributed generation (DG) scheme [1–3]. Thanks to the development of power electronic components and power converter topologies, and on the other hand the availability of digital signal processors incorporating dedicated units, the implementation of islanded and grid-connected micro-grids, including renewable energy sources, has become possible and manageable [4, 5]. During grid-connected mode, the inverters can act as a current source (i.e. grid-feeding) or as a voltage source (i.e. grid-forming). Operating a power inverter in grid-forming mode using the droop control strategy has recently seen much focus as the transition between the grid-connected and islanded operating modes does not require control reconfiguration and the MG can seamlessly disconnect from the grid [6, 7]. In such a control mode, the main objective is to ensure proper active and reactive power flow between the inverter and the utility grid. However, the actual measured active and reactive powers are mandatory when the droop control strategy is adopted. Unfortunately, the commonly

applied method for power calculations in droop-controlled grid-interactive inverters is based on a low-pass filter (LPF) to achieve the average power. The major drawback of this method is the lack of speed since an LPF with a low cutoff frequency is required to reject the undesirable distortions [8]. This issue may degrade the control performance, thus threatening the correct operation of grid-connected inverters. On the other hand, in most of the related research papers that have addressed the modelling of grid-interactive droop-controlled inverters, the LPF transfer function is generally adopted to describe the dynamics of the power computation. Such an option might not be valid for single-phase systems, where the estimation dynamic of the components required for power calculation should be considered. In this regard, considering an advanced control scheme, effective modelling, and stability assessment of droop-controlled grid-tied inverters with enhanced power calculation methods and taking into consideration properly its dynamics should be addressed.

In droop-controlled inverters, the active and reactive powers are generally calculated in the $\alpha\beta$ frame by using the voltage and current orthogonal components ($v_{\alpha\beta}$, $i_{\alpha\beta}$) [9]. These components are obtained through the *abc*-to-$\alpha\beta$ transformation in a three-phase system, whereas in a single-phase system, an additional unit is required for generating the quadrature component (v_{β}). The extraction of the average active and reactive powers is performed by an LPF, with a low cutoff frequency, which filters out the inherent oscillation power component resulting from power calculation [8–10]. However, the use of such a filter may decrease the velocity of the power calculation, hence degrading the transient performance of the droop control. To deal with this issue, the authors in [11] have adopted a real-time integration method, instead of using an LPF, to obtain the average power in a three-phase grid-tied inverter. In [12], a band-pass filter (BPF) has been considered for power calculation for a droop-controlled single-phase inverter. Another effective solution that has been used for power computation in single-phase systems is the second-order generalized integrator frequency-locked loop (SOGI-FLL) method [13–16]. Although this method has provided an improvement in the droop control dynamic response in terms of speed and accuracy, the presence of the DC disturbance, which may appear in the grid voltage and current, might degrade the performance of the orthogonal component estimates, hence threatening the power calculation accuracy. To overcome such a problem, advanced methods based on SOGI-FLL, such as enhanced second-order generalized integrator frequency-locked loop (ESOGI-FLL), n-SOGI, and pre-filtering-SOGI, are proposed in the literature to deal with the DC-offset issue and improve further the performance of the power calculation [8, 17]. These methods have shown their effectiveness in terms of power computation with high accuracy, fast transient response, high harmonics, and DC components rejection capabilities as well as low computational burdens. Nevertheless, the application of such methods has been considered only for droop-controlled inverters within islanded microgrids, whereas for droop-controlled inverters operating in grid-connected mode, they have not been applied yet.

On the other hand, the modelling and stability assessment of grid-forming inverters have been addressed in several research works [11, 18–21]. For instance, in [11] and [18], a small-signal model and stability assessment of a single-phase inverter connected to the main grid has been provided. The authors in [19] have addressed the small-signal modelling and analysis of a droop-controlled inverter operating in grid-tied mode. Furthermore, the small-signal modelling of a grid-forming inverter in single-phase MG has been adopted in [20] and [21]. However, in these modelling approaches, the authors often consider the assumption that the line impedance is highly inductive, then assuming its corresponding resistance negligible. Such an assumption might be valid for systems with high transmission lines, but in DG systems, it is not a valid assumption. In this regard, the modelling of grid-forming inverters taking into consideration line impedance with R/X ratio has been adopted in the literature. For instance, the authors in [22] and [23] have modelled a single inverter interfaced stiff grid taking into consideration the R/X ratio. In addition, a state-space model of a single-phase droop-operated grid-tied inverter considering a complex line impedance is presented in [24]. Further, modelling and stability assessment based on dynamic phasors for droop-controlled inverters has been addressed in [25] to achieve a precise mathematical model by considering the R/X ratio. Moreover, in [26] dynamic phasors-based modelling approach for droop-controlled grid-tied inverters has been developed taking into account a complex line impedance. In all the stated works, a first-order transfer function of the LPF is introduced for describing the power calculation dynamics. However, in single-phase systems, such a concept might not be valid since the dynamic of the orthogonal component estimate should be considered. As a result, the accuracy of the derived models may be questionable, and the stability of the system is compromised.

To deal with the aforementioned issues, the design of an advanced control scheme, modelling, and analysis of droop-controlled grid-connected inverters-based MG are developed in this paper. The following contributions are made in this paper:

- An advanced control scheme of the power flow which includes an enhanced SOGI-FLL-based power calculation strategy is designed. The ESOGI-FLL offers a fast transient response, a total rejection of DC offset capability, effective filtering of the grid voltage and current harmonics, and a low computational burden. This makes the power calculation scheme immune to DC disturbance and leads to improving the speed and accuracy of power computation, thereby enhancing the power flow control performance.
- A dynamic phasor modelling approach of a droop-controlled grid-interactive inverter considering the ESOGI-FLL-based power calculation dynamics is developed. In this modelling approach, the state-space small-signal model of the power flow of a single-phase grid-tied VSI considering power coupling is first derived. Second, the model that describes the dynamics of the power calculation based on ESOGI-FLL is extracted and its accuracy is verified. By merging these models, the small-signal open-loop of grid-connected VSI

power flow is obtained and its accuracy is assessed through numerical case studies in the MATLAB environment.
- A procedure for obtaining the closed-loop small-signal model of the whole system incorporating a proportional-integral (PI) power controller is established. Thanks to this model, the system stability is effectively investigated and the power controllers' gains are determined.

MATLAB/Sim Power System and PSIM's PIL simulation tests are carried out to assess the effectiveness and robustness of the developed control approach. The obtained results are presented showing the performance of the designed controllers in ensuring proper operation of the grid-connected VSI under various grid abnormalities.

The rest of this paper is arranged as follows. In Section 2, the power control scheme proposed based on droop control for a single-phase grid-tied VSI is provided. The modelling approach based on dynamic phasors is developed in Section 3. In this section, the state-space model of the power flow and dynamic of the ESOGI-FLL-based power calculations are derived and validated. In addition, the closed-loop model of the power control-based grid-tied VSI system is obtained. The investigation of the grid-connected VSI stability and controller's robustness assessment are presented in Section 4. In Section 5, the simulation results and discussion are provided. Section 6 reports the main conclusions of the paper.

2 | PROPOSED CONTROL SCHEME FOR GRID-TIED DROOP-CONTROLLED VSIs

In grid-connected droop-controlled inverters, an LPF is often employed to achieve the average active and reactive power needed by the power controller (or droop control). This concept may slow down the transient response of the droop control. In addition, the effect of the DC component that may appear in the output voltage cannot be also handled by using LPF. To deal with these issues, a power control scheme that includes an ESOGI-FLL-based power calculation technique intended for droop-controlled grid-connected inverters within a single-phase MG is adopted. Figure 1 shows the control scheme including the proposed power control intended for a single-phase grid-forming inverter. As shown in this figure, an inverter with an LC filter is connected to the main utility grid via a line impedance. Also, a load is linked to the point of common coupling (PCC), where the power generated by the DC source through VSI is injected. The control scheme consists of two essential control loops. A dual-loop inner controller for regulating the inverter's output voltage, in which the inner loop adjusts the current of the LC filter, and the capacitor voltage is controlled by the outer loop. This controller provides the inverter voltage reference, v^*_{inv}, divided by the measured DC source voltage, and the resulted duty cycle reference, D^*, is then entered into the PWM that in turn generates the VSI's switches commands. A proposed power control, which has a slower transient response compared to the voltage and current control loops, is responsible for generating the reference of the output voltage of the inverter and synchronizing to the main utility grid. This control block includes two main units: an ESOGI-FLL-based power calculation unit and power controllers. The ESOGI-FLL, which is characterized by its simplicity of implementation and DC-offset rejection and harmonics filtering capabilities [17], is introduced to estimate accurately the direct and quadrature components of the inverter's output current and grid voltage. These estimated components are used to compute the real and reactive power, $\hat{P}$ and $\hat{Q}$, in the $\alpha\beta$-frame by using (1). The power controllers are in charge of regulating the real and reactive power references according to the corresponding calculated actual powers. Then, the produced voltage frequency and amplitude, f and E, are used to generate the voltage reference by using a sine generator.

$$P = \frac{1}{2}\left(\hat{v}_{g-\alpha} \times \hat{i}_{\alpha} + \hat{v}_{g-\beta} \times \hat{i}_{\beta}\right)$$
$$Q = \frac{1}{2}\left(\hat{v}_{g-\beta} \times \hat{i}_{\alpha} - \hat{v}_{g-\alpha} \times \hat{i}_{\beta}\right) \quad (1)$$

being $\hat{i}_{\alpha,\beta}$ and $\hat{v}_{g-\alpha,\beta}$ the in-phase and in-quadrature phase fundamental components of the output current and grid voltage estimated by the ESOGI-FLL, respectively.

The structure of the ESOGI-FLL is illustrated in Figure 2, which involves two main blocks, ESOGI and FLL. The ESOGI consists of a standard SOGI with an LPF for DC component estimation/rejection. This block is responsible for estimating the in-phase and in-quadrature phase components of a single-phase input voltage v. The FLL is in charge of detecting the centre frequency ω used for the tune of the ESOGI block. The transfer functions of the in-phase $\hat{v}_{\alpha}$ and in-quadrature phase without DC-offset, $\hat{v}_{\beta}$, which both exhibit BPFs, and of the in-quadrature component with DC-offset, $\hat{v}_{\beta-dc}$, which exhibit an LPF are given as follows:

$$G_{\alpha}(s) = \frac{\hat{v}_{\alpha}(s)}{v(s)} = k\hat{\omega}\frac{s}{s^2 + k\hat{\omega}s + \hat{\omega}^2} \quad (2)$$

$$G_{\beta}(s) = \frac{\hat{v}_{\beta}(s)}{v(s)} = \frac{k\left(\hat{\omega}^2 - \omega_f s\right)}{s + \omega_f}\frac{s}{s^2 + k\hat{\omega}s + \hat{\omega}^2} \quad (3)$$

$$G_{\beta-dc}(s) = \frac{\hat{v}_{\beta-dc}(s)}{v(s)} = \frac{k\hat{\omega}^2}{s^2 + k\hat{\omega}s + \hat{\omega}^2} \quad (4)$$

where k represents the filters' damping factor, which is selected as a tradeoff between the time response and harmonics filtering properties, and ω_f is the cutoff frequency of the LPF. For more details about the ESOGI-FLL and the dual-loop inner control, refer to [17] and [6], respectively.

The expression of the real and reactive power controllers can be written as follows [19]:

$$\omega = \omega_n - k_{p-P}\left(\hat{P} - P^*\right) - k_{i-P}\int\left(\hat{P} - P^*\right)dt - k_{d-P}/dt^d\left(\hat{P} - P^*\right)$$
$$E = E_n - k_{p-Q}\left(\hat{Q} - Q^*\right) - k_{i-Q}\int\left(\hat{Q} - Q^*\right)dt \quad (5)$$

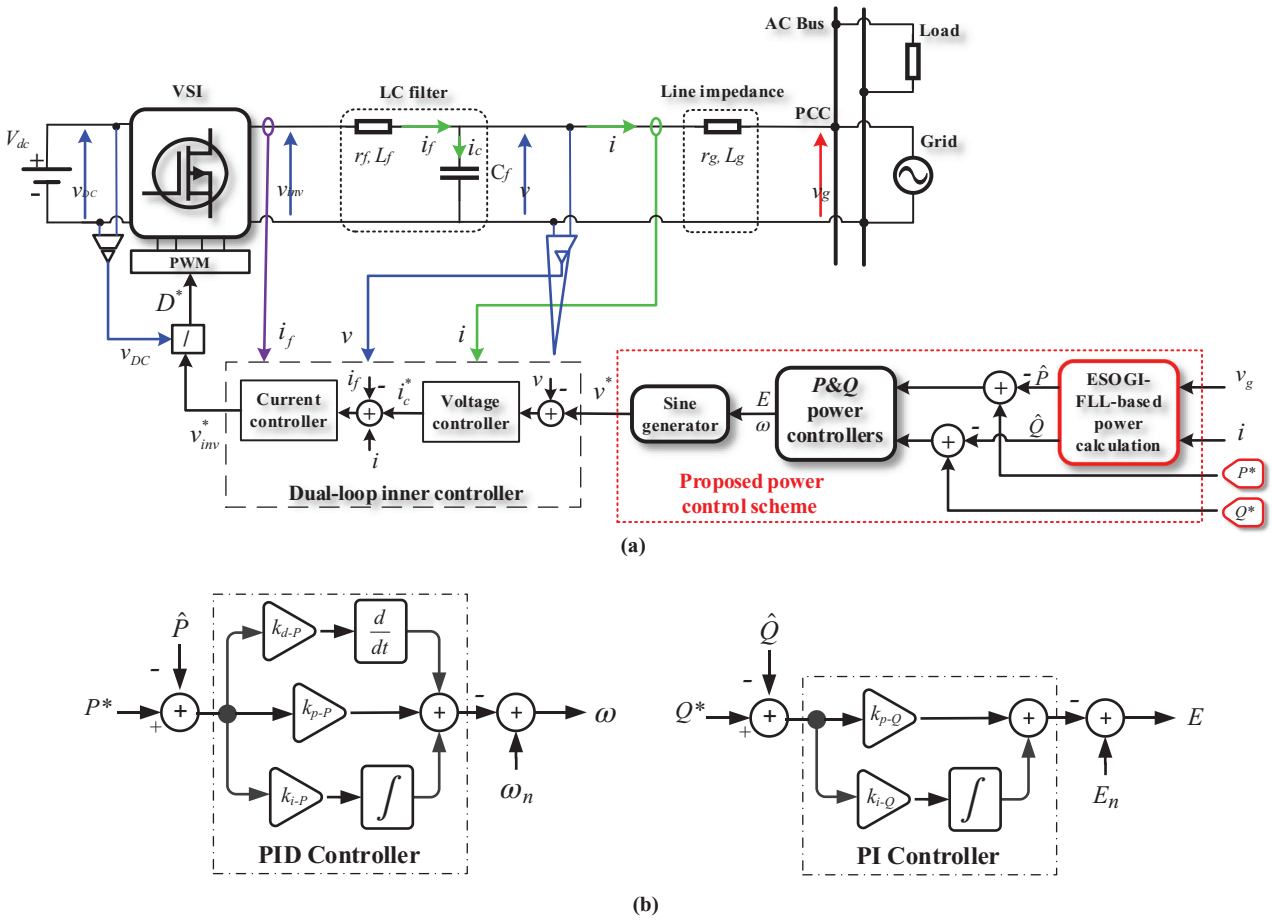

FIGURE 1 Schematic diagram of: (a) the proposed power control scheme for a single-phase grid-tied inverter, and (b) the active and reactive power controllers

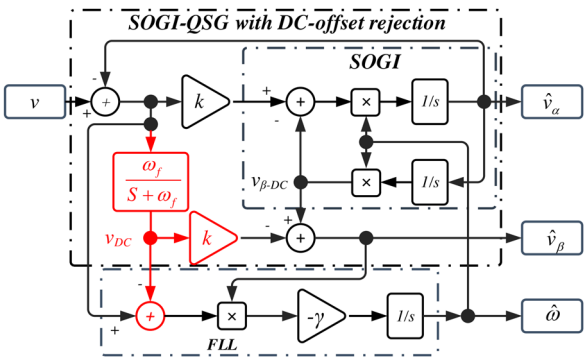

FIGURE 2 Structure of the ESOGI-FLL

where $k_{p\text{-}P}$, $k_{i\text{-}P}$, $k_{d\text{-}P}$, $k_{p\text{-}Q}$, and $k_{i\text{-}Q}$ are the gains of the power controllers, and $\hat{P}$, $\hat{Q}$, P^*, and Q^* are the estimated real and reactive powers by the ESOGI-based power calculation block, and their references (* refers to the reference value of a variable). And ω, E, ω_n, and E_n denote the frequency and amplitude of the inverter output voltage and their nominal values, respectively. In addition, the schematic diagram of the active and reactive power controllers' implementation is shown in Figure 1b, in which the PID and PI controllers are considered for the active and reactive power control, respectively.

In such an operating condition, the grid will determine the frequency of the inverter so that this action will change the power angle. A similar procedure can be considered for the reactive power according to the voltage inverter amplitude E. It is worth noting that, when the islanded mode occurs the inverter is disconnected from the main grid for safety, and the integral gains of the power control are set to zero. This control strategy contributes to allowing a smooth transition between grid-tied and autonomous operation modes.

To study the stability of the grid-tied inverter-based MG incorporating power control as well as determine properly the parameter of the power controller, a mathematical model is needed. Thus, in the next section, a modelling approach based on dynamic phasors is proposed to extract the expected model.

3 | PHASOR MODELLING OF A GRID-TIED DROOP-CONTROLLED VSI

This section focuses on developing a small-signal model of a grid-tied single-phase inverter controlled by the droop method, by using the dynamic phasors. The block diagram of the whole

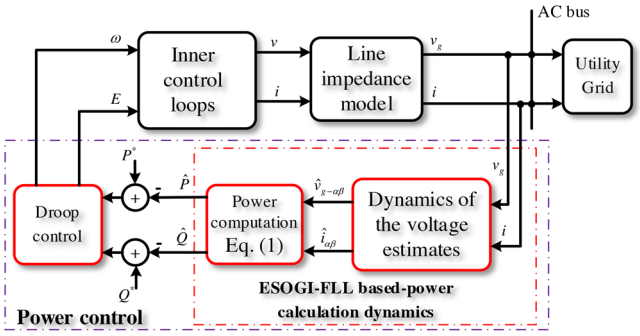

FIGURE 3 Model of the whole system including the power control dynamics

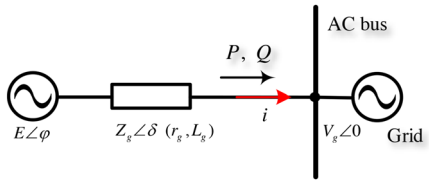

FIGURE 4 Simplified circuit of a VSI interfaced to AC utility grid

system model is shown in Figure 3. According to this figure, the system model involves the droop control functions, the model of the line impedance that describes the changes of the frequency and amplitude at the AC bus, and the ESOGI-FLL-based power calculation dynamics. In addition, it includes the model of the dual-loops current and voltage controllers of the inverter, which are considered negligible due to their higher bandwidth than the droop controller. To achieve the expected small-signal model of the overall system, the modelling of each stage within the system under study is developed hereafter.

3.1 | Mathematical expression of the power flows through the line impedance

Figure 4 illustrates the simplified circuit of a VSI linked to the main utility grid via a tie line impedance. The VSI is represented by a controlled AC source where harmonic content is negligible. The grid is modelled as an independent voltage source ($V_g\angle 0$).

According to this circuit, the complex power S injected into the grid is given by the following expression :

$$S = v_g \times \bar{i} = V_g\angle 0 \left(\frac{V_g\angle 0 - E\angle\varphi}{Z_g\angle\delta} \right) = P + jQ \tag{6}$$

where i is the injected current into the main grid, φ is the phase angle of the inverter voltage, Z and δ are the magnitude and phase of the line impedance, j defines the imaginary operator of a complex number, and $\bar{}$ denotes the complex conjugate operator, respectively.

To obtain the mathematical formulation of the complex power (or the real and reactive powers), the first expression in (6) is used, in which the expression of the line impedance current, i, should be determined first.

Based on the equivalent circuit given in Figure 4, the electrical equation relating the inverter's voltage $v(t)$ to the output current, $i(t)$, and the grid voltage, $v_g(t)$, can be derived in the time domain, as follows:

$$v(t) = r_g i(t) + L_g \frac{di(t)}{dt} + v_g(t) \tag{7}$$

where r_g and L_g are the resistive and inductive components of the line impedance, respectively.

In the phasor domain, a sinusoidal voltage $v(t) = V \times \cos(\omega t + \theta)$; with amplitude V, angular frequency ω, and initial phase θ, can be represented by [26]

$$v(t) = \sqrt{2}\mathrm{Re}\left\{ V_{dq} e^{j\omega t} \right\} \tag{8}$$

where V_{dq} is the phasor voltage in the rotating reference frame (dq), given by

$$V_{dq} = \frac{1}{\sqrt{2}} V e^{j\theta} \tag{9}$$

By applying this concept, (7) can be rewritten in dq-frame, after some mathematical manipulation, as follows:

$$E_{dq} = r_g I_{dq} + L_g \frac{dI_{dq}}{dt} + jL_g\omega I_{dq} + V_{g-dq} \tag{10}$$

Consequently, the expression of the line impedance current (I_{dq}) in the s-domain, where s is the Laplace operator, can be described by

$$I_{dq}(s) = \frac{E_{dq}(s) - V_{g-dq}(s)}{L_g s + r_g + jL_g\omega} \tag{11}$$

On the other hand, the grid voltage $V_{g\text{-}dq}$ and the inverter's output voltage E_{dq} in dq-frame can be defined in the time domain, considering the power-invariant Park transformation [27], as follows:

$$\begin{cases} E_{dq} = \sqrt{\frac{3}{2}} E\angle\varphi \\ V_{g-dq} = \sqrt{\frac{3}{2}} V_g\angle 0 \end{cases} \tag{12}$$

Accordingly, the expression of the line impedance current can be obtained, in the s-domain, as follows:

$$i(s) = \sqrt{\frac{3}{2}} \frac{\left(E\angle\varphi - V_g\angle 0\right)\left(L_g s + r_g - jL_g\omega\right)}{\left(r_g + L_g s\right)^2 + \left(L_g\omega\right)^2} \tag{13}$$

By substituting the expression of the line impedance current (13) into (6), the expressions of the real and reactive power can

be obtained as follows:

$$\begin{cases} P = \dfrac{3}{2}\dfrac{L_g s + r_g}{\left(L_g s + r_g\right)^2 + \left(L_g\omega\right)^2}\left(V_g E\cos(\varphi) - V_g^2\right) \\ \quad + \dfrac{3}{2}\dfrac{L_g\omega}{\left(L_g s + r\right)^2 + \left(L_g\omega\right)^2} V_g E\sin(\varphi) \\ Q = \dfrac{3}{2}\dfrac{L_g\omega}{\left(L_g s + r_g\right)^2 + \left(L_g\omega\right)^2}\left(V_g E\cos(\varphi) - V_g^2\right) \\ \quad - \dfrac{3}{2}\dfrac{\left(L_g s + r_g\right)}{\left(L_g s + r_g\right)^2 + \left(L_g\omega\right)^2}\cdot V_g E\sin(\varphi) \end{cases} \tag{14}$$

For the sake of simplicity, (14) can be rewritten as follows:

$$\begin{cases} P = \dfrac{r_g + L_g s}{\left(r_g + L_g s\right)^2 + \left(L_g\omega\right)^2} u_2 + \dfrac{L_g\omega}{\left(r_g + L_g s\right)^2 + \left(L_g\omega\right)^2} u_1 \\ Q = \dfrac{L_g\omega}{\left(r_g + L_g s\right)^2 + \left(L_g\omega\right)^2} u_2 - \dfrac{\left(r + L_g s\right)}{\left(r_g + L_g s\right)^2 + \left(L_g\omega\right)^2} u_1 \end{cases} \tag{15}$$

with

$$u_1 = \frac{3}{2} V_g E\sin(\varphi), \quad u_2 = \frac{3}{2}\left(V_g E\cos(\varphi) - V_g^2\right) \tag{16}$$

On the other side, the real and reactive power (15) can be defined in a matrix form as a function of a state variable x as follows:

$$\begin{bmatrix} P \\ Q \end{bmatrix} = \begin{bmatrix} L_g\omega & L_g s + r_g \\ -\left(L_g s + r_g\right) & L_g\omega \end{bmatrix} \begin{bmatrix} x_1 \\ x_2 \end{bmatrix} \tag{17}$$

in which the expression relating the state variable x to the vector u can be given by

$$\begin{bmatrix} x_1 \\ x_2 \end{bmatrix} = \frac{1}{s^2 + 2\frac{r_g}{L_g} s + \left(\frac{r_g}{L_g}\right)^2 + \omega^2} \begin{bmatrix} \frac{1}{L_g^2} & 0 \\ 0 & \frac{1}{L_g^2} \end{bmatrix} \begin{bmatrix} u_1 \\ u_2 \end{bmatrix} \tag{18}$$

By merging (17) and (18), the mathematical model of the real and reactive power flow can be presented in state-space representation as

$$\begin{cases} \begin{bmatrix} \dot{x}_1 \\ \ddot{x}_1 \\ \dot{x}_2 \\ \ddot{x}_2 \end{bmatrix} = \begin{bmatrix} 0 & 1 & 0 & 0 \\ -\left(\left(\frac{r_g}{L_g}\right)^2 + \omega^2\right) - \left(2\frac{r_g}{L_g}\right) & 0 & 0 \\ 0 & 0 & 0 & 1 \\ 0 & 0 & -\left(\left(\frac{r_g}{L_g}\right)^2 + \omega^2\right) - \left(2\frac{r_g}{L_g}\right) \end{bmatrix} \\ \quad \begin{bmatrix} x_1 \\ \dot{x}_1 \\ x_2 \\ \dot{x}_2 \end{bmatrix} + \begin{bmatrix} 0 & 0 \\ \frac{1}{L_g^2} & 0 \\ 0 & 0 \\ 0 & \frac{1}{L_g^2} \end{bmatrix} \begin{bmatrix} u_1 \\ u_2 \end{bmatrix} \\ \quad \begin{bmatrix} P \\ Q \end{bmatrix} = \begin{bmatrix} L_g\omega & 0 & r_g & L_g \\ -r_g & -L_g & L_g\omega & 0 \end{bmatrix} \begin{bmatrix} x_1 \\ \dot{x}_1 \\ x_2 \\ \dot{x}_2 \end{bmatrix} \end{cases} \tag{19}$$

where $(\dot{x})$ and $(\ddot{x})$ denote the first derivate and the second derivate of state vector x, respectively.

By linearizing (19) around the equilibrium points, E_{eq}, φ_{eq}, and V_g, the state-space small-signal model of the real and reactive power flow can be obtained as follows:

$$\begin{cases} \begin{bmatrix} \Delta\dot{x}_1 \\ \Delta\ddot{x}_1 \\ \Delta\dot{x}_2 \\ \Delta\ddot{x}_2 \end{bmatrix} = \begin{bmatrix} 0 & 1 & 0 & 0 \\ -\left(\left(\frac{r_g}{L_g}\right)^2 + \omega^2\right) - \left(2\frac{r_g}{L_g}\right) & 0 & 0 \\ 0 & 0 & 0 & 1 \\ 0 & 0 & -\left(\left(\frac{r_g}{L_g}\right)^2 + \omega^2\right) - \left(2\frac{r_g}{L_g}\right) \end{bmatrix} \\ \quad \begin{bmatrix} \Delta x_1 \\ \Delta\dot{x}_1 \\ \Delta x_2 \\ \Delta\dot{x}_2 \end{bmatrix} + \begin{bmatrix} 0 & 0 \\ \frac{k_{11}}{L_g^2} & \frac{k_{12}}{L_g^2} \\ 0 & 0 \\ \frac{k_{21}}{L_g^2} & \frac{k_{22}}{L_g^2} \end{bmatrix} \begin{bmatrix} \Delta\varphi \\ \Delta E \end{bmatrix} \\ \quad \begin{bmatrix} \Delta P \\ \Delta Q \end{bmatrix} = \begin{bmatrix} L_g\omega & 0 & r_g & L_g \\ -r_g & -L_g & L_g\omega & 0 \end{bmatrix} \begin{bmatrix} \Delta x_1 \\ \Delta\dot{x}_1 \\ \Delta x_2 \\ \Delta\dot{x}_2 \end{bmatrix} \end{cases} \tag{20}$$

where Δ represents the small variation of a variable from the equilibrium point, and the parameters k_{11}, k_{12}, k_{21}, and k_{22} can

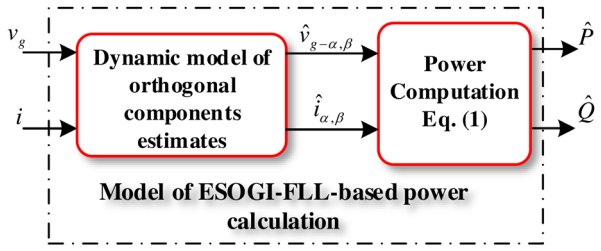

FIGURE 5 Model of power calculation based on the ESOGI-FLL dynamics

be determined according to the following equation:

$$\begin{bmatrix}\Delta u_1\\ 36pt]\Delta u_2\end{bmatrix} = \begin{bmatrix}k_{11} & k_{12}\\ k_{21} & k_{22}\end{bmatrix}\begin{bmatrix}\Delta\varphi\\ \Delta E\end{bmatrix} = \frac{3}{2}V_g\begin{bmatrix}E_{eq}\cos(\varphi_{eq}) & \sin(\varphi_{eq})\\ -E_{eq}\sin(\varphi_{eq}) & \cos(\varphi_{eq})\end{bmatrix}\begin{bmatrix}\Delta\varphi\\ \Delta E\end{bmatrix} \quad (21)$$

In addition, based on (16), the values of the equilibrium points, E_{eq} and φ_{eq}, can be calculated by using the following expressions:

$$\varphi_{eq} = Arctg\left(\frac{2u_{1n}}{2u_{2n}+3V_g^2}\right),$$
$$E_{eq} = \sqrt{\left(\frac{2}{3}\frac{u_{1n}}{V_g}\right)^2 + \left(\frac{2}{3}\frac{u_{2n}}{V_g}+V_g\right)^2} \quad (22)$$

where the expression of the vector u, at the equilibrium point, as a function of P^* and Q^* can be determined according to (17) and (18), after setting s to zero, as follows:

$$\begin{bmatrix}u_{1n}\\ u_{2n}\end{bmatrix} = \left[r_g^2+(L_g\omega)^2\right]\begin{bmatrix}L_g\omega & r_g\\ -r_g & L_g\omega\end{bmatrix}^{-1}\begin{bmatrix}P^*\\ Q^*\end{bmatrix} \quad (23)$$

The state-space small-signal model given by (20) expresses the dynamics of the real and reactive power flow to change in the voltage phase angle and magnitude inputs considering the R/X ratio of line impedance Z_g.

The second model that should be derived is the one that describes the dynamics of the power calculation based on the ESOGI-FLL method.

3.2 | Modelling of the ESOGI-FLL-based power calculation

As mentioned earlier, the average real and reactive power are calculated by using the ESOGI-FLL outputs corresponding to the fundamental component. The block diagram of the power calculation model including the ESOGI-FLL dynamics is presented in Figure 5.

It is well known that the real and reactive power corresponding to fundamental frequency, taking into consideration $V_{g\text{-}d}$ as a reference in the rotating reference frame (i.e. $V_{g\text{-}q}=0$), can be defined as follows [28]:

$$\begin{cases}\hat{P} = V_{g-d}\times\hat{I}_d\\ \hat{Q} = -V_{g-d}\times\hat{I}_q\end{cases} \quad (24)$$

being I_d and I_q the output current direct and quadrature components and $V_{g\text{-}d}$ is the direct component of the grid voltage given in (12).

According to (24), the estimated powers are expressed by the current estimates of the ESOGI-FLL, and their dynamics should be derived. To achieve these dynamics, the same mathematical analysis based on the dynamic phasor modelling presented in [29], for obtaining the mathematical model that describes the voltage estimate of the SOGI, is considered. Hence, based on the transfer functions of $\hat{v}_\alpha$ and $\hat{v}_{\beta-dc}$ estimates given by (2) and (4), the expression of the estimated orthogonal components of the output current can be obtained in a rotating reference frame as follows:

$$\begin{bmatrix}\hat{I}_d\\ \hat{I}_q\end{bmatrix} = k\omega\frac{\left[s^3+k\omega s^2+2\omega^2 s+k\omega^3\right]}{\left[s(s+k\omega)\right]^2+\left[\omega(2s+k\omega)\right]^2}\begin{bmatrix}I_d\\ I_q\end{bmatrix} \quad (25)$$

This expression stands for the dynamic of current estimation based on the ESOGI-FLL.

Merging (24) and (25), the transfer function relating the estimated real and reactive power, $\hat{P}$ and $\hat{Q}$, to the actual ones, P and Q, can be derived, after some mathematical manipulation, as follows:

$$\begin{cases}\hat{P} = \left(\frac{k\omega\times s^3+k^2\omega^2\times s^2+2k\omega^3\times s+k^2\omega^4}{s^4+2k\omega\times s^3+(k^2\omega^2+4\omega^2)s^2+4k\omega^3\times s+k^2\omega^4}\right)P\\ \hat{Q} = \left(\frac{k\omega\times s^3+k^2\omega^2\times s^2+2k\omega^3\times s+k^2\omega^4}{s^4+2k\omega\times s^3+(k^2\omega^2+4\omega^2)s^2+4k\omega^3\times s+k^2\omega^4}\right)Q\end{cases} \quad (26)$$

This transfer function expresses the dynamics of the real and reactive power estimates based on the ESOGI-FLL technique.

where the transfer functions $H_p(s)$ and $H_q(s)$ denote LPFs of fourth-order, given by

$$H_p(s) = H_q(s) = H(s) = \frac{k\omega\times s^3+k^2\omega^2\times s^2+2k\omega^3\times s+k^2\omega^4}{s^4+2k\omega\times s^3+(k^2\omega^2+4\omega^2)s^2+4k\omega^3\times s+k^2\omega^4} \quad (27)$$

To facilitate the modelling analysis and control design, the transfer function $H(s)$ can be approximated to a first-order transfer function. By considering the same mathematical analysis presented in [29], the first-order transfer function that corresponds to the one given by (28) is

$$H(s) = \frac{\Delta\hat{P}}{\Delta P} = \frac{1/2k\omega}{s+1/2k\omega} \quad (28)$$

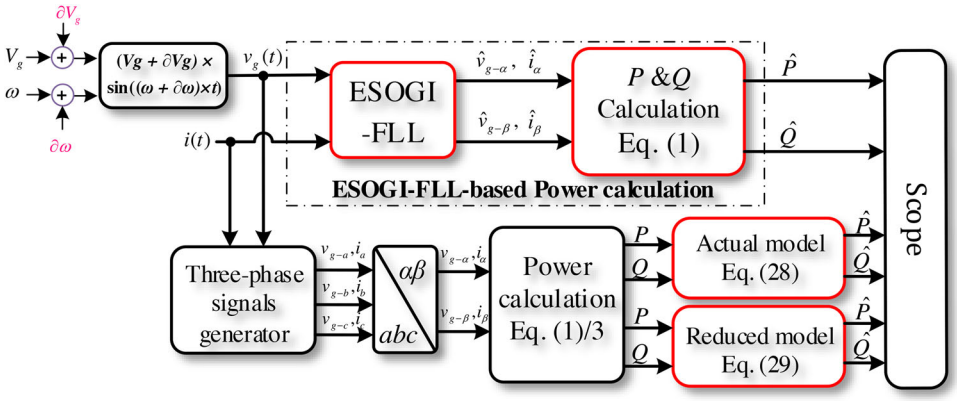

FIGURE 6 Block diagram of the simulated testbed in MATLAB for the models' validation

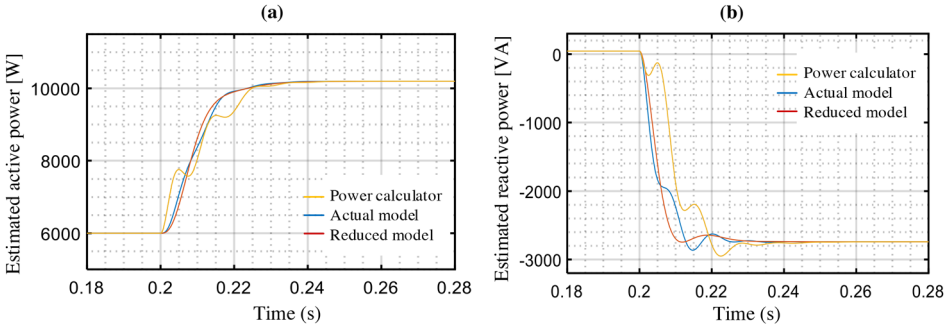

FIGURE 7 Investigating the accuracy of the actual and the reduced models to f variation

This transfer function defines the reduced small-signal model of the real power computation dynamics based on the ESOGI-FLL.

3.2.1 | Accuracy assessment of the obtained model

To investigate the accuracy of the derived actual and the reduced models of the real and reactive power computation, given by (28) and (29), a simulation study in the MATLAB/Simulink^{TM} is performed considering some standard tests. Figure 6 shows the test platform simulated in MATLAB, in which, as mentioned earlier, the ESOGI-FLL-based structure is involved for real and reactive power calculations. But, as seen in Figure 6, the inputs actual powers of the obtained models are measured in the $\alpha\beta$ reference frame by using (1). The *abc*-to-$\alpha\beta$ transformation is applied to generate three-phase signals, and then to transfer them to the orthogonal $\alpha\beta$ components. In this study, the provided active and reactive powers by the ESOGI-FLL-based power calculator are compared to the ones predicted by the obtained models in response to step changes in the input voltage frequency and amplitude, with an amount of ∂V_g and $\partial\omega$. The transient performance of the P and Q estimates for frequency and amplitude changes, respectively, are illustrated in Figures 7 and 8. As shown, the calculated real and reactive powers are varied at $t = 0.2$ s, corresponding to the voltage frequency and amplitude increase. In addition, one can see that the scopes of the produced powers by the models are matched with the provided powers by the power calculation block. Hence, the actual and the reduced models, as demonstrated, are able to predict accurately the ESOGI-FLL-based power calculation average behaviour.

As a result, the obtained models are very useful to be integrated into the power flow modelling for describing the active and reactive power calculation dynamics.

Note that we use the computation of powers in a three-phase balanced system (based on the product of harmonic-free voltage and current), because it provides constant instantaneous powers, unlike in the case of a single phase, where it produces oscillating instantaneous real and reactive powers [30].

3.3 | Open-loop model of the grid-tied VSI power flow

The open-loop small-signal model is the one that relates the estimated real and reactive powers to the voltage phase angle and amplitude. This model, shown in Figure 9, is obtained by merging the model of the grid-tied VSI power flow, given by (20), and the approximated small-signal model describing the power calculation dynamics, given by (29). Accordingly, the linearized open-loop small-signal model of the real and reactive power is expressed in state-space form, after some mathematical

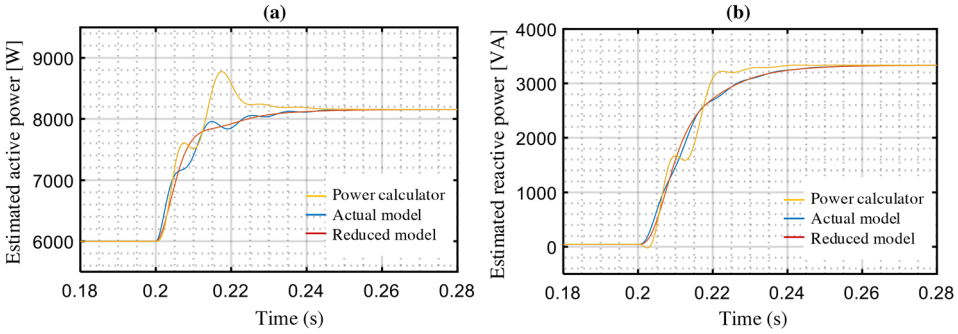

FIGURE 8 Investigating the accuracy of the actual and the reduced models to E variation

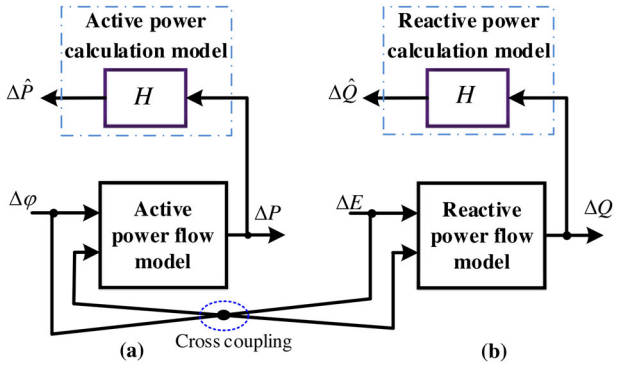

FIGURE 9 Open-loop model of: (a) real and (b) reactive power flow

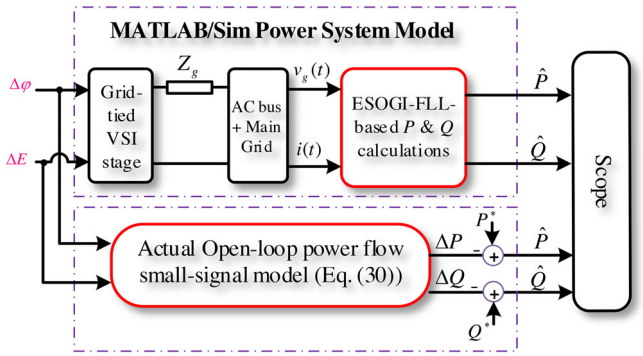

FIGURE 10 Schematic diagram of the implemented system in MATLAB sim power system

manipulations, as follows:

$$
\begin{cases}
\begin{bmatrix} \Delta\dot{x}_1 \\ \Delta\ddot{x}_1 \\ \Delta\dddot{x}_1 \\ \Delta\dot{x}_2 \\ \Delta\ddot{x}_2 \\ \Delta\dddot{x}_2 \end{bmatrix} = \begin{bmatrix} 0 & 1 & 0 & 0 & 0 & 0 \\ 0 & 0 & 1 & 0 & 0 & 0 \\ -a_1 & -a_2 & -a_3 & 0 & 0 & 0 \\ 0 & 0 & 0 & 0 & 1 & 0 \\ 0 & 0 & 0 & 0 & 0 & 1 \\ 0 & 0 & 0 & -a_1 & a_2 & a_3 \end{bmatrix} \begin{bmatrix} \Delta x_1 \\ \Delta\dot{x}_1 \\ \Delta\ddot{x}_1 \\ \Delta x_2 \\ \Delta\dot{x}_2 \\ \Delta\ddot{x}_2 \end{bmatrix} \\
\quad + \frac{k\omega}{2L_g^2} \begin{bmatrix} 0 & 0 \\ 0 & 0 \\ k_{11} & k_{12} \\ 0 & 0 \\ 0 & 0 \\ k_{21} & k_{22} \end{bmatrix} \begin{bmatrix} \Delta\varphi \\ \Delta E \end{bmatrix} \\
\begin{bmatrix} \Delta P \\ \Delta Q \end{bmatrix} = \begin{bmatrix} L_g\omega & 0 & 0 & r_g & L_g & 0 \\ -r_g & -L_g & L_g\omega & 0 & 0 & 0 \end{bmatrix} \begin{bmatrix} \Delta x_1 \\ \Delta\dot{x}_1 \\ \Delta\ddot{x}_1 \\ \Delta x_2 \\ \Delta\dot{x}_2 \\ \Delta\ddot{x}_2 \end{bmatrix}
\end{cases}
\tag{29}
$$

where the parametersa_1, a_2, and a_3 are given by

$$
\begin{aligned}
a_1 &= -k\omega/2\left(\left(\frac{r_g}{L_g}\right)^2 + \omega^2\right), \\
a_2 &= -\left(\frac{k\omega r_g}{L_g} + \left(\frac{r_g}{L_g}\right)^2 + \omega^2\right), \\
a_3 &= -\left(2\frac{r_g}{L_g} + k\omega/2\right)
\end{aligned}
\tag{30}
$$

3.3.1 | Model verification

The accuracy investigation of the open-loop small-signal model of the grid-forming inverter power flow is verified under phase angle and amplitude voltage variations. In this investigation, simulation tests are carried out based on the schematic in Figure 10. The testbed is a single-phase VSI linked to the AC bus with the power-based ESOGI-FLL block. The transfer function of the obtained model is implemented in MATLAB SimPowerSystem™. The results showing the dynamic performance of the estimated powers by the analytic model compared to the ones delivered by the single-phase VSI power stage are shown in Figures 11, and prove the model's accuracy.

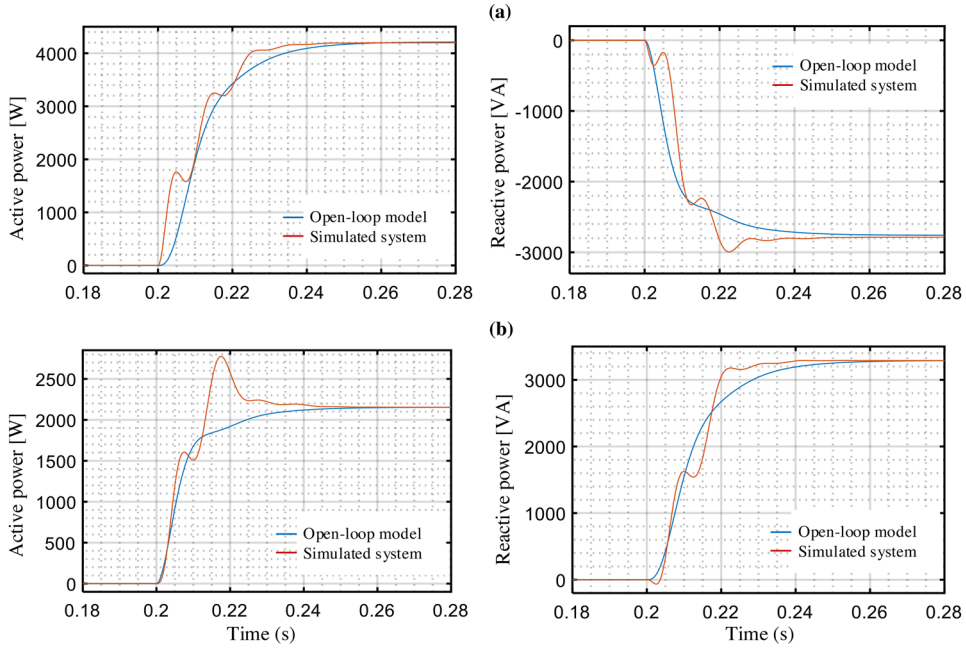

FIGURE 11 *P* and *Q* transient responses for step-change in the voltage: (a) phase angle, and (b) amplitude

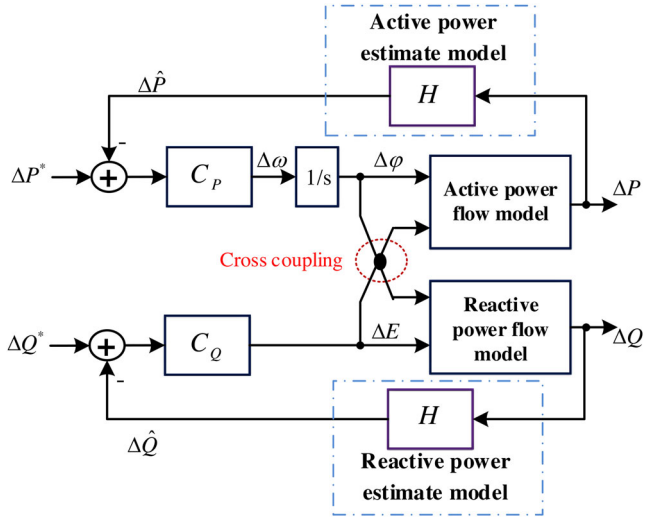

FIGURE 12 Closed-loop small-signal model of the grid-tied VSI incorporating power control

3.4 | Closed-loop small-signal model of grid-tied VSI incorporating power control

The closed-loop small-signal model of the whole system is shown in Figure 12. This model consists of the model of the power flow through the impedance of the line, the dynamics of the ESOGI-FLL-based power calculation ($H_{p,q}(s)$), and the droop controller ($C_{p,q}(s)$).

To obtain the mathematical expression of the closed-loop model, we assume that the reactive power reference is set to zero that is, $Q^* = 0$. Therefore, the expression of the droop control (given by (5)) under small variations can be rewritten in the *s*-domain as follows:

$$\Delta\varphi = C_P(s)/s\left(\Delta P^* - \Delta\hat{P}\right) \tag{31.a}$$

$$\Delta E = -C_Q(s)\,\Delta\hat{Q} \tag{31.b}$$

where C_P and C_Q are defined as follows:

$$C_P(s) = \frac{k_{p-P}s + k_{i-P} + k_{d-P}s^2}{s},\quad C_Q(s) = \frac{k_{p-Q}s + k_{i-Q}}{s} \tag{32}$$

In addition, by combining and linearizing (17) and (18) around operating points, the expression relating the real and reactive power to the vector *u* can be derived as

$$\begin{bmatrix}\Delta P\\ \Delta Q\end{bmatrix} = \begin{bmatrix}G_1 & G_2\\ -G_2 & G_1\end{bmatrix} \times \begin{bmatrix}\Delta u_1\\ \Delta u_2\end{bmatrix} \tag{33}$$

where G_1 and G_2 are given by

$$G_1 = \frac{L_g\omega}{r_g^2 + \left(L_g\omega\right)^2}, G_2 = \frac{r_g}{r_g^2 + \left(L_g\omega\right)^2} \tag{34}$$

Merging (34) and (21), the expression relating small variations of the real and reactive power to the voltage frequency and amplitude can be defined as follows:

$$\begin{bmatrix}\Delta P\\ \Delta Q\end{bmatrix} = \begin{bmatrix}G_1 & G_2\\ -G_2 & G_1\end{bmatrix}\begin{bmatrix}k_{11} & k_{12}\\ k_{21} & k_{22}\end{bmatrix}\begin{bmatrix}\Delta\varphi\\ \Delta E\end{bmatrix} \tag{35}$$

On the other side, the mathematical expression describing the dynamics of the actual powers to the estimated ones can

be rewritten in matrix form as follows:

$$\begin{bmatrix} \Delta\hat{P} \\ \Delta\hat{Q} \end{bmatrix} = H \begin{bmatrix} \Delta P \\ \Delta Q \end{bmatrix} \tag{36}$$

By substituting (37) into (36), the expression of the small variations of the estimated powers corresponding to the phase angle and voltage variations can be obtained as

$$\begin{bmatrix} \Delta\hat{P} \\ \Delta\hat{Q} \end{bmatrix} = H \begin{bmatrix} G_1 & G_2 \\ -G_2 & G_1 \end{bmatrix} \begin{bmatrix} k_{11} & k_{12} \\ k_{21} & k_{22} \end{bmatrix} \begin{bmatrix} \Delta\varphi \\ \Delta E \end{bmatrix} = \begin{bmatrix} G_{11} & G_{12} \\ G_{21} & G_{22} \end{bmatrix} \begin{bmatrix} \Delta\varphi \\ \Delta E \end{bmatrix} \tag{37}$$

Based on this equation (38) and (32.b), the transfer function relating the variations of the amplitude to the phase angle can be represented by

$$\Delta E = -\frac{C_Q G_{21}}{(C_Q G_{22} + 1)} \Delta\varphi \tag{38}$$

By substituting into (38), the transfer function describing the dynamics of the real power estimate to the phase angle variations can be given by

$$\Delta\hat{P} = \left(G_{11} - \frac{C_Q G_{12} G_{21}}{(C_Q G_{22} + 1)} \right) \Delta\varphi \tag{39}$$

Consequently, the closed-loop small-signal model of the active power control can be expressed by

$$\Delta\hat{P} = \left(G_{11} - \frac{C_Q G_{12} G_{21}}{(C_Q G_{22} + 1)} \right) \times \frac{\frac{C_P}{s}}{1 + \frac{C_P}{s} \left(G_{11} - \frac{C_Q G_{12} G_{21}}{(C_Q G_{22} + 1)} \right)} \Delta P^* \tag{40}$$

This model is useful to study the stability of droop-controlled grid-connected VSI and for the tuning of the power controllers' parameters.

4 | STABILITY ANALYSIS, CONTROL DESIGN, AND ROBUSTNESS ASSESSMENT

This section investigates the control design-based stability analysis of the power flow control and the robustness assessment of the designed controller by using the obtained closed-loop model.

4.1 | Stability analysis and control parameters' tuning

In order to determine the power controller gains, the stability of the grid-connected droop-controlled VSI is assessed by using the obtained closed-loop model. The characteristic equation roots of the actual model (41) are evaluated to power controller parameters' variations ($k_{p\text{-}P}$, $k_{i\text{-}P}$, $k_{d\text{-}P}$, $k_{p\text{-}Q}$, and $k_{i\text{-}Q}$). The trajectory of the roots of the closed-loop model when the active power ($k_{p\text{-}P}$, $k_{i\text{-}P}$, $k_{d\text{-}P}$) and reactive power ($k_{p\text{-}Q}$ and $k_{i\text{-}Q}$) control parameters vary is shown in Figures 13 and 14, respectively. In these figures, the black arrows depict the poles' increasing trend and the red symbol (x) denotes the poles' initial value. According to the roots' plots in Figures 13a, 13b, and 13c, one can observe that a pair of complex poles move towards the unstable region as $k_{p\text{-}P}$, $k_{i\text{-}P}$, and $k_{d\text{-}P}$ increase, leading the grid-tied VSI system to instability issues. Hence, the system is stable as long as $k_{p\text{-}P}$, $k_{i\text{-}P}$, and $k_{d\text{-}P}$ are less than the values 0.91×10^{-4}, 0.02, and 1.56×10^{-5}, respectively. In addition, as shown in Figures 14a and 14b, the increase of $k_{p\text{-}Q}$ and $k_{i\text{-}Q}$ shifts a pair of complex poles towards the positive real region, hence making the system unstable if $k_{p\text{-}Q}$ and $k_{i\text{-}Q}$ are superior to the values 0.0053 and 0.183, respectively.

4.2 | Robustness assessment

To verify the robustness of the designed power controller, simulation tests are carried out in MATLAB based on the obtained closed-loop power flow model given by (41). In this simulation study, the controller is tested against system parameter variations considering the following case studies:

- **Case 1**: when the line resistance (r_g) varied in the range of $0.1 \times r_g \leq r_g \leq 5 \times r_g$
- **Case 2**: when the line inductance (L_g) varied in the range of $0.5 \times L_g \leq L_g \leq 10 \times L_g$
- **Case 3**: the frequency (ω) varied in the range of $0.1 \times \omega \leq \omega \leq 2 \times \omega$.

It is worth noting that the values of r_g, L_g, and ω are initially set to 200 Ω, 2 mH, and 50 Hz, respectively.

The roots evaluation of the closed-loop model characteristic equation when varying the resistance (r_g) and inductance (L_g) of the interconnected line, as well as the inverter operating frequency (ω), is illustrated in Figures 15a, 15b, and 15c, respectively. According to this figure, it is clearly shown that the gird-connected VSI system is stable for a specified values range of the considered parameter. One can observe in Figure 15a that the system is stable in the range where the line resistance r_g belongs to the interval of $0.7 \times r_g$ to $4.6 \times r_g$. While, out of this range, two poles move to the positive real side of the s-plane; making the system unstable. One can see in Figure 15b that when the line inductance L_g values belong to the range of $0.9 \times L_g < L_g < 5 \times L_g$, the system is stable. Nevertheless, out of this range, several poles move to the unstable region and as a result, the grid-connected VSI system stability is questionable. From

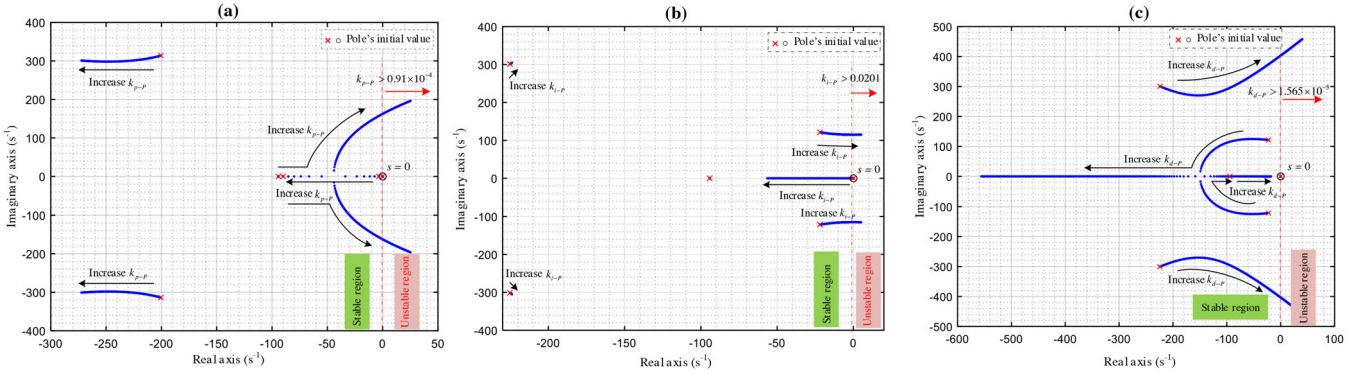

FIGURE 13 Root-Locus plots for: (a) $10^{-5} \leq k_{p\text{-}P} \leq 0.0015$ and $k_{i\text{-}P} = k_{d\text{-}P} = k_{p\text{-}Q} = k_{i\text{-}Q} = 0$, (b) $10^{-5} \leq k_{i\text{-}P} \leq 0.025$ and $k_{p\text{-}P} = 5\times10^{-4}$, $k_{d\text{-}P} = k_{p\text{-}Q} = k_{i\text{-}Q} = 0$, and (c) $5 \times 10^{-8} \leq k_{d\text{-}P} \leq 2.5 \times 10^{-5}$ and $k_{p\text{-}P} = 5 \times 10^{-4}$, $k_{i\text{-}P} = 10^{-4}$, $k_{p\text{-}Q} = k_{i\text{-}Q} = 0$

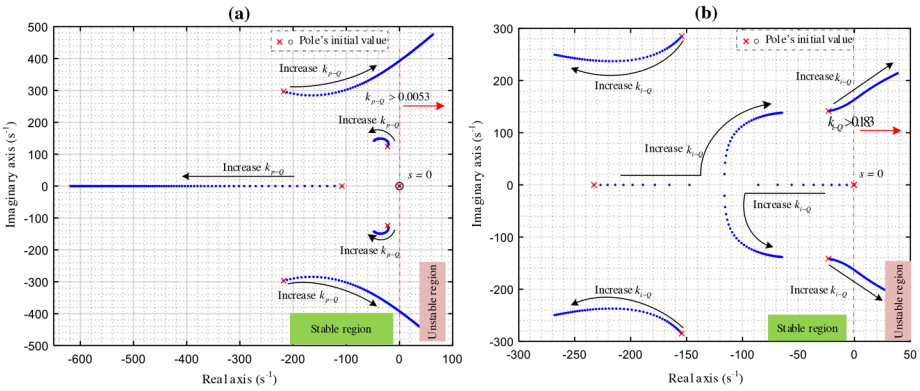

FIGURE 14 Root-Locus plots for: (a) $10^{-4} \leq k_{p\text{-}P} \leq 0.01$ and $k_{p\text{-}P} = 5 \times 10^{-4}$, $k_{i\text{-}P} = 10^{-4}$, $k_{d\text{-}P} = 10^{-7}$, $k_{i\text{-}Q} = 0$, and (b) $10^{-3} \leq k_{i\text{-}Q} \leq 0.5$, $k_{p\text{-}P} = 5 \times 10^{-4}$, $k_{i\text{-}P} = 10^{-4}$, $k_{d\text{-}P} = 10^{-7}$, $k_{p\text{-}Q} = 0.001$

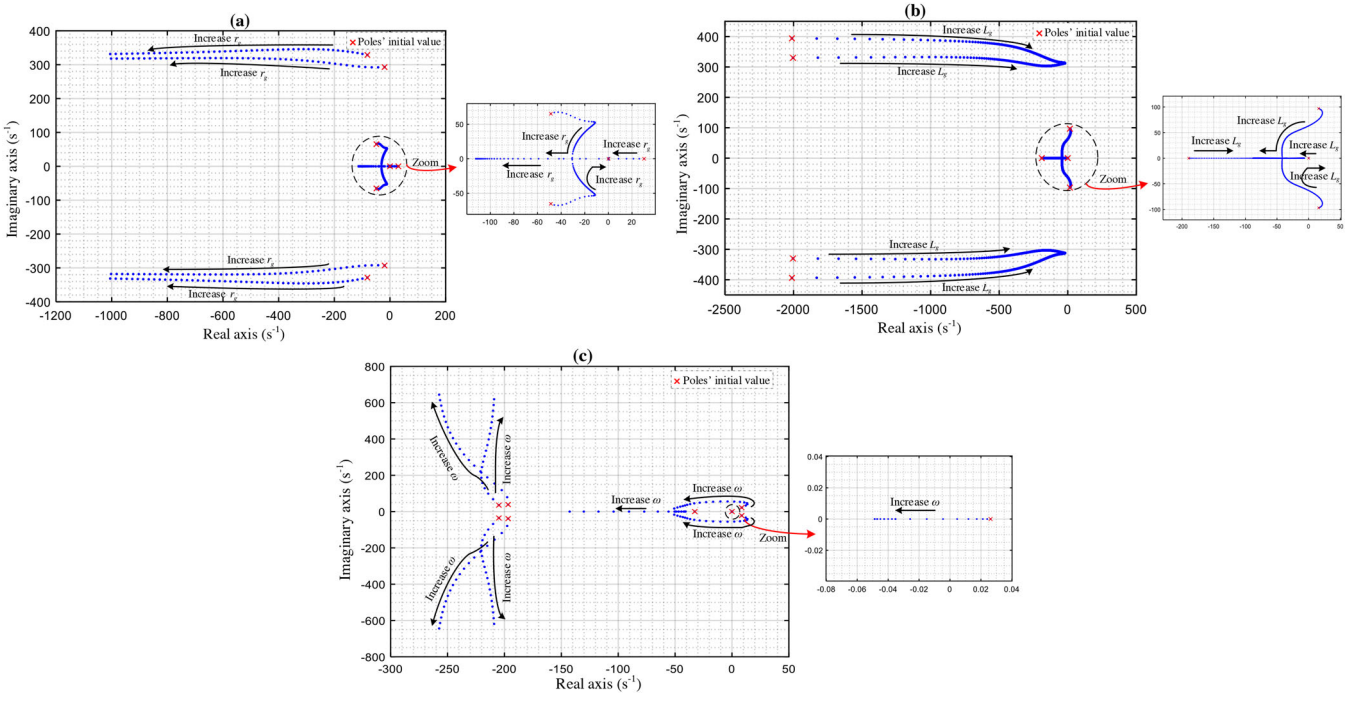

FIGURE 15 Family of the eigenvalues of the obtained closed-loop model for: (a) line resistance variation and zoom, (b) line inductance variation and zoom, and (c) frequency variation and zoom

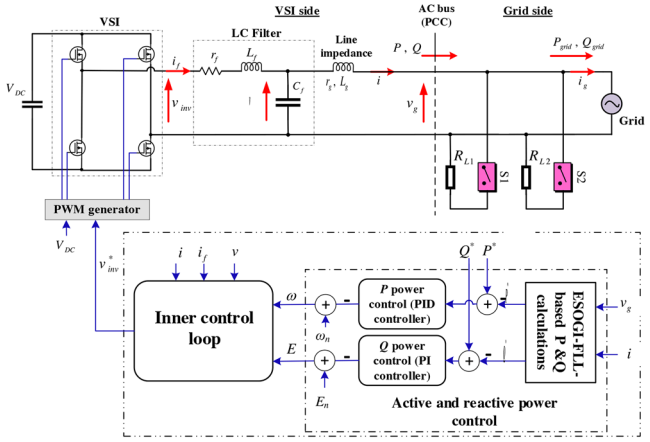

FIGURE 16 A testbed of a single-phase grid-connected VSI, with the proposed power control

Figure 15c, one can be noticed that when the value of the operating frequency is changed in the range of $0.6 \times \omega < \omega < 1.03 \times \omega$, the system is stable, and else, it indicates unstable conditions for the system. Consequently, the obtained results confirm the robustness of the designed controller versus a wide range of system parameters.

TABLE 1 Parameters of the power stage and power control

Parameters	Symbol	Unit	Value
Power stage			
Nominal voltage (RMS)	E_n (RMS)	V	220
Nominal frequency	$\omega_n/2\pi$	Hz	50
DC bus voltage	V_{DC}	V	495
Filter capacitor	C_f	μF	23
Filter inductor	r_f, L_f	Ω, mH	1, 2
Line impedance of DG #1	L_g, r_g	mH, Ω	1.5, 0.01
Loads (RL1, RL2)	R_L, L_L	Ω, mH	100, 15
SOGI-FLL unit			
SOGI damping factor	K	–	0.6
FLL gain	Γ	s^{-1}	40
Power control			
P proportional gain	$k_{p\text{-}P}$	–	5×10^{-4}
P integral gain	$k_{i\text{-}P}$	s^{-1}	0.0001
P derivate gain	$k_{d\text{-}P}$	–	1.036×10^{-7}
Q proportional gain	$k_{p\text{-}Q}$	–	0.001
Q integral gain	$k_{i\text{-}Q}$	–	0.05

5 | SIMULATION RESULTS AND DISCUSSIONS

To assess the proposed control strategy, an H-bridge single-phase inverter associated with an LC filter to remove high-frequency harmonics is adopted as a testbed. This inverter is tied to the utility grid via a coupling impedance as shown in Figure 16. The utility grid is considered, in this simulation study, as a voltage-controlled source to mimic some state abnormalities. The simulation study is conducted under MATLAB/Simulink/SimPowerSystem™. The proposed power control scheme is introduced to regulate the real and reactive power injected into the main grid. The simulation parameters are given in Table 1. To confirm robustness against DC disturbance which occurs in signal measurements the value of the DC component in the measurement is set to 0.03 p. u from the voltage amplitude.

The effectiveness of the proposed control scheme is assessed assuming five representative tests

- **Test 1**: Sudden change in P^*:
- bullet-from 1 to 1.5 kW at $t = 2$ s
- bullet-from 1.5 to 1 kW at $t = 4$ s
- **Test 2**: Sudden change in Q^* from 0 to 50 VAR is set at $t = 2$ s.
- **Test 3**: A grid voltage sag of 0.01 p. u (from the grid fundamental amplitude) form $t = 1.5$ to $t = 3$ s), is set.
- **Test 4**: The grid phase angle is changed with the amount of $\pi/100$ at $t = 2$ s.
- **Test 5**: The proposed controller is assessed in front of load changes. To this end, an inductive load (RL1) with $R = 100$ Ω and $L = 15$ mH is suddenly connected on the grid side at $t = 1.5$ s, and another inductive load (RL2) with the same value is connected at $t = 3$ s.

The obtained results given in Figures 17–21 highlight the main performances of the grid-connected VSI based on the proposed power control. These figures depict the time evolution of actual real and reactive powers generated by the VSI and their references. In addition, they show the frequency, amplitude, voltage, and current of the VSI side and grid side transient responses. Figures 17a to 17c display the responses to active power reference change. As shown in Figure 17a, during the period from $t = 0$ to 2 s, the power controller precisely regulates the active and reactive power, P and Q, provided by the inverter to their references, P^* and Q^* (1 kW and = 0 VAR). Meanwhile, as illustrated in Figure 17b, the inverter frequency f_{VSI} is matched to grid frequency (f_{Grid} = 50 Hz), whereas a teeny difference between the amplitude of the inverter E_{VSI} and the grid (E_{Grid} = 1 p. u, i.e. 220 V (RMS)) due to the line impedance is observed. Further, from Figure 17c, it can be seen that pure sinusoidal waveforms of the inverter side and the grid side voltages (v_{VSI}, v_g) and currents (i_{VSI}, i_g) are obtained. When changing the active power reference, P^*, at t = 2s, the active power P successfully tracks the new desired value, as depicted in Figure 17a. In addition, it can be noticed that a seamless transient response with a settling time around 0.5 s and without overshoot is achieved.

Further, it can be seen that the reactive power Q is set to its reference 0 VAR, with a slight transient when varying the active power. From Figure 17b, it can be seen that the inverter frequency f_{VSI} changes when P varies, and comes back to

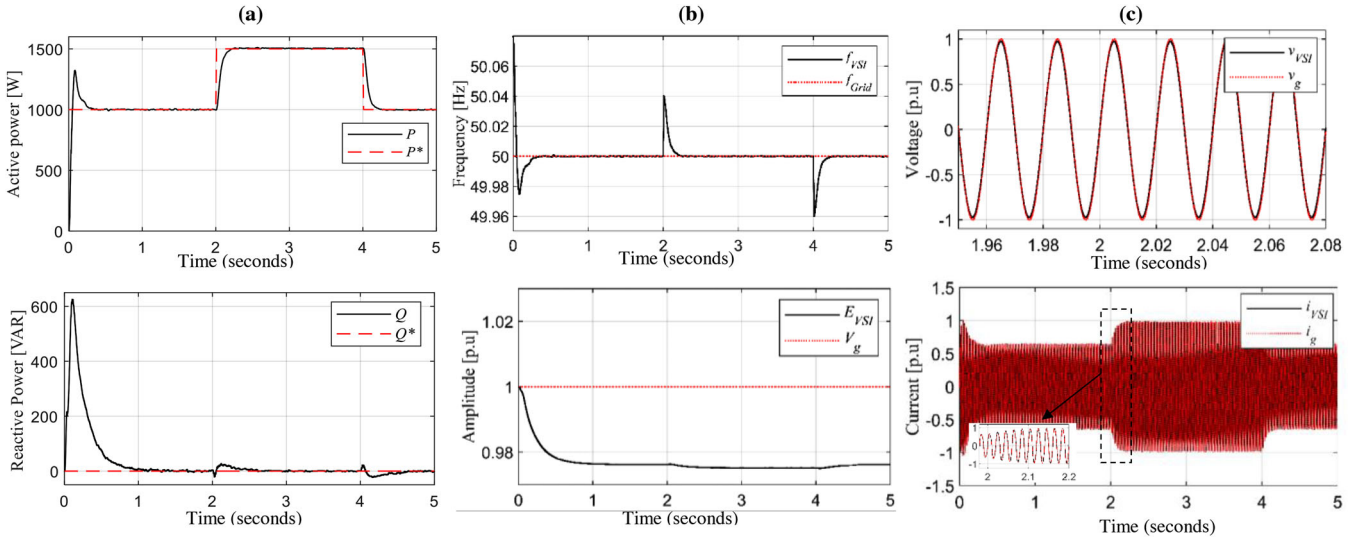

FIGURE 17 Obtained results in response to test 1

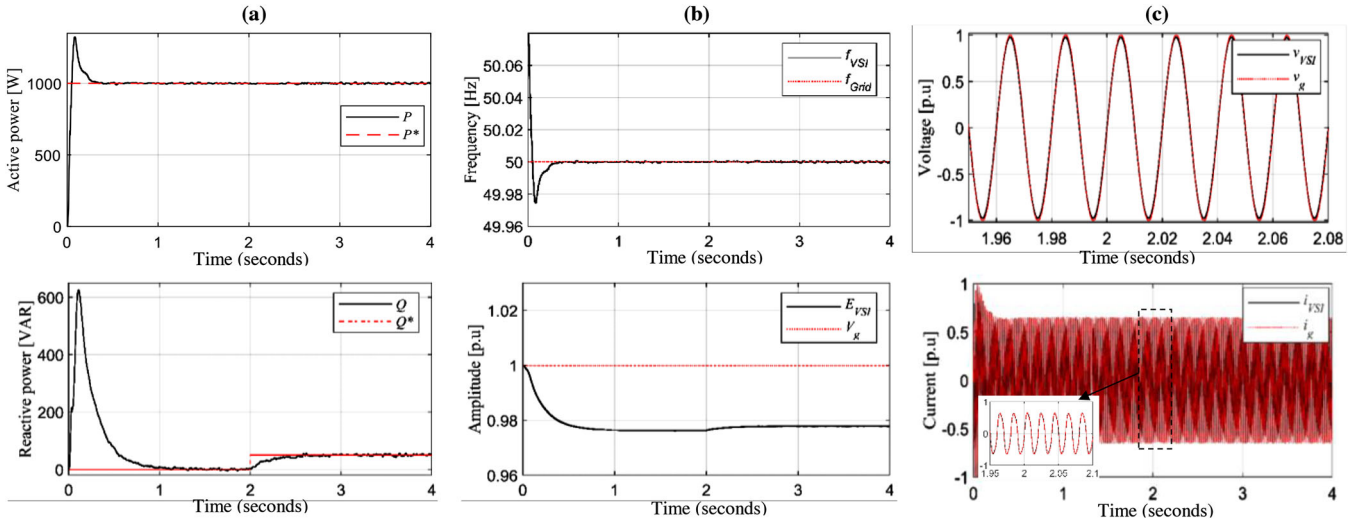

FIGURE 18 Obtained results in response to test 2

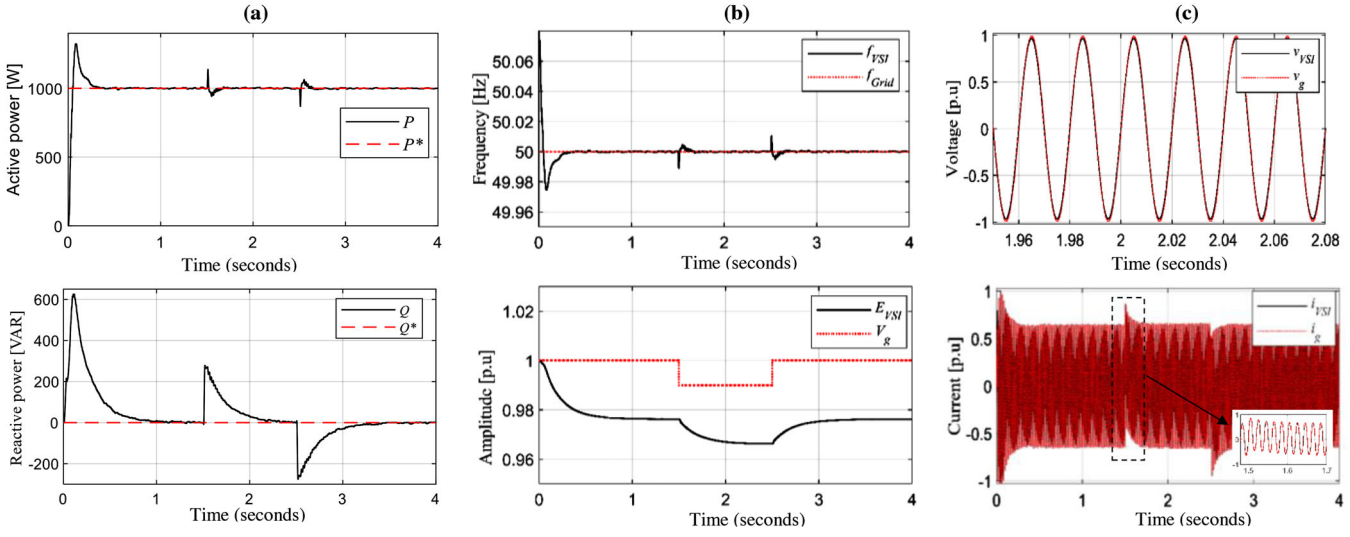

FIGURE 19 Obtained results in response to voltage sag (test 3)

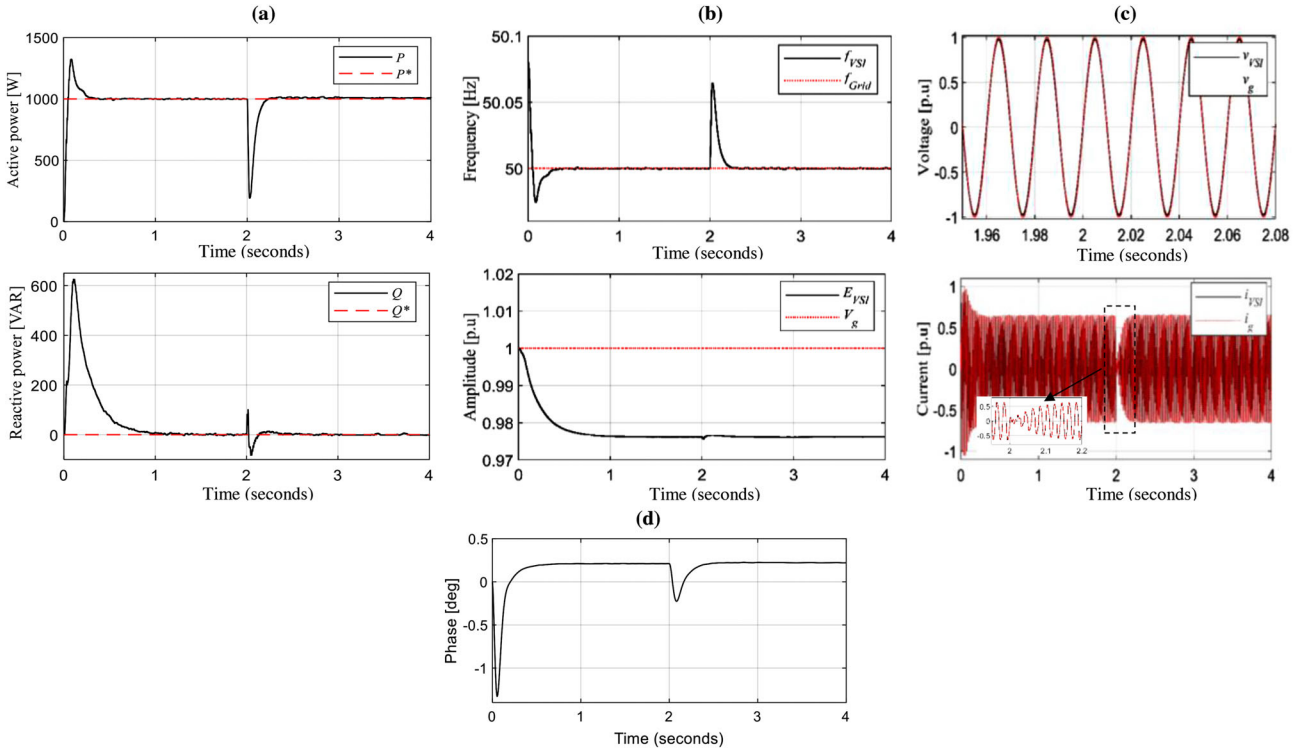

FIGURE 20 Obtained results in response to test 4

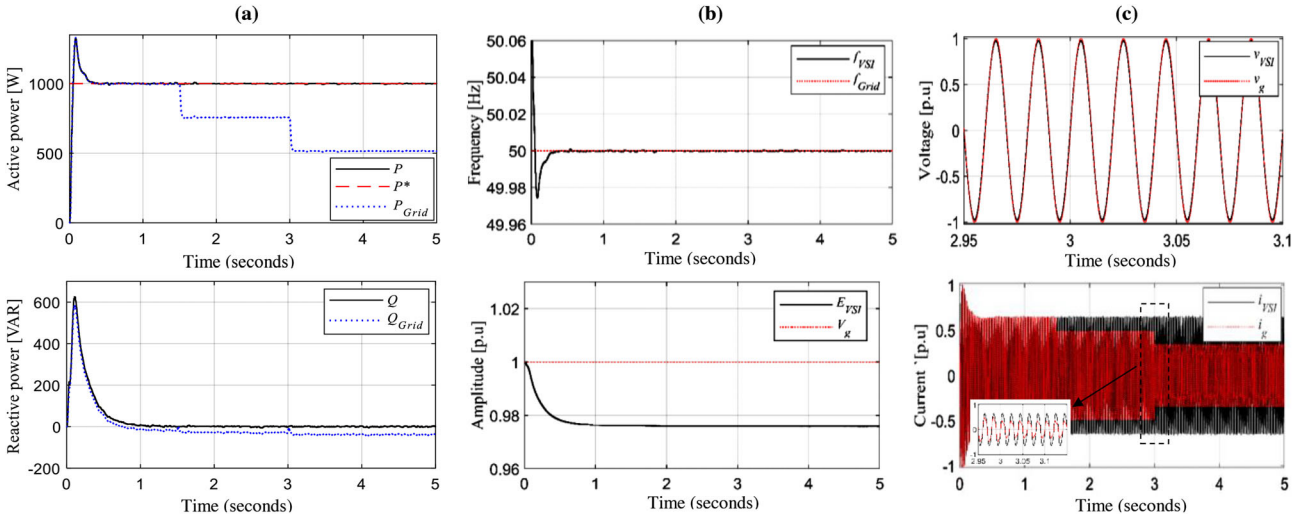

FIGURE 21 Obtained results in response to test 5

synchronize with the grid frequency f_{Grid}. While the amplitude of the inverter, E_{VSI}, remains almost unchanged. Furthermore, according to Figure 17c, the current of the inverter i_{VSI} increases as the power demand grows, while the grid current i_g follows the inverter current (i_{VSI}). in addition, the voltage of the grid side and inverter side, v_g and v_{VSI}, keep their amounts constants. Further, the injection of proper sinusoidal currents into the grid is observed, as illustrated in the zoom of Figure 17c. The same discussions are considered, at $t = 4$ s, when P^* comes back to the reference value of 1 kW. The results in Figure 18 show the responses of the proposed power controller to Q^* step change. From Figure 18a, one can see that when Q^* changes at $t = 2$ s, the proposed controller smoothly adjusts the reactive power Q to its new reference; that is, 50 VAR. This is done with a settling time $t_s = 0.5$ s and without oscillations. Meanwhile, P is fixed to its reference value during all the simulation time even when Q^* vary. The transient response presented in Figure 18b illustrates that the inverter frequency f_{VSI} remains unchanged and matches with the grid frequency f_{Grid}. Also one can notice that the voltage amplitude E_{VSI} increases with a tinny amount corresponding to the reactive power change. Further, it can be noted that the current and voltage of the inverter side and the

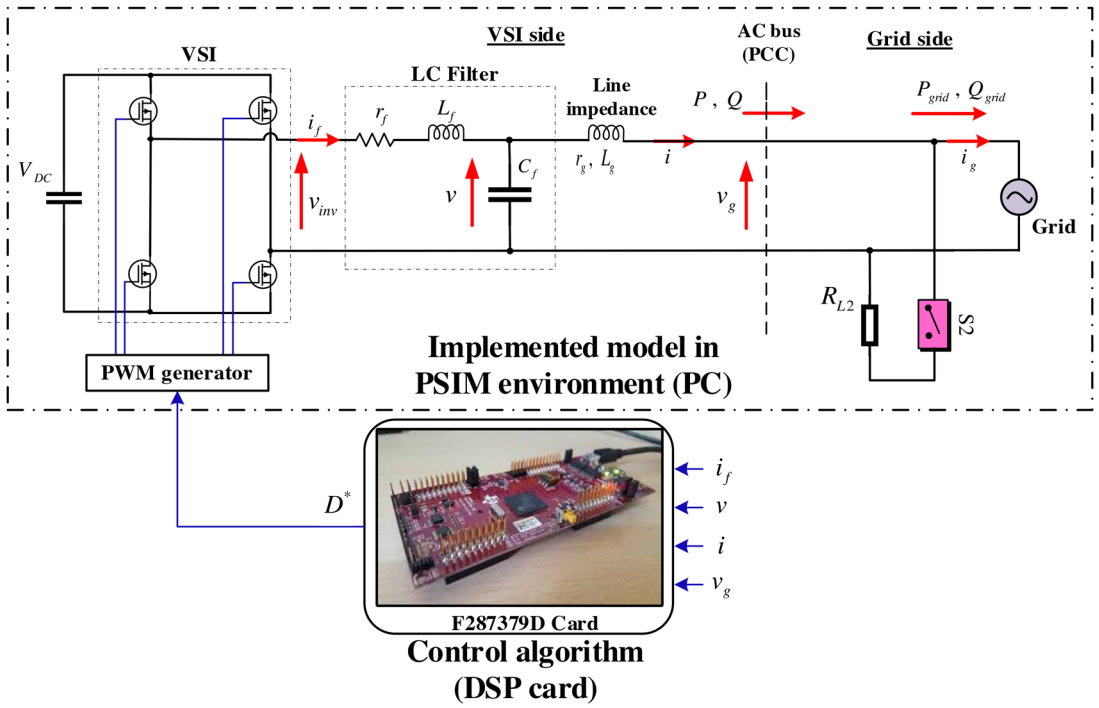

FIGURE 22 PIL simulation model in PSIM. PIL, processor in the loop

grid side, shown in Figure 18c, almost remain unchanged, with pure sinusoidal waveforms.

The transient responses of the proposed power controller for grid voltage dip are shown in Figure 19. When the grid voltage sag appears during $t = 1.5$ s to $t = 2.5$ s, P and Q are fixed by the power controller to their references, but with a slight transient in P and proper transient in Q, as can be seen in Figure 19a. From Figure 19b, it can be noticed that the f_{VSI} remains unchanged, just with a slight transient when v_{VSI} changes. Also the amplitude transient response shows that E_{VSI} follows the dripped grid amplitude with a constant error between them. According to Figure 19c, it can be remarked that voltages of the grid side and inverter side keep their pure sinusoidal forms, in which their dips, during this period, cannot be noticed due to their tinny amount. In addition, one can see that the grid and inverter currents remain unchanged, just with a transient at the time when the grid voltage slops.

The results in Figure 20 present the power control performance in response to the grid phase jump. From Figure 20a, it can be observed that the controller forces the inverter to operate at its desired P^*, in which a transient is noticed when the grid phase is jumped. Also, we note that the controller fixes the Q to its reference (0 VAR), just with slight oscillations under phase jump. The responses given in Figure 20b demonstrate that f_{VSI} varies, when the phase jumps, then backs match with f_g. From this figure, we noticed, also, that E_{VSI} almost remains unchanged. Furthermore, from Figure 20c, it can be seen that v_{VSI} remains constant and synchronizes with v_g. Also it can be remarked that the currents i_{VSI} and i_g keep their sinusoidal forms, just with a noticeable transient during the grid phase jump. Moreover, the response of the phase angle between the inverter side and the grid side is depicted in Figure 20d. From this figure, one can note that there is a tenny constant phase between the grid and the inverter due to the line impedance. In addition, it can be noticed that this phase angle varied; when the grid phase jumped; and then returns to its previous value.

Figure 21 presents the performance of the proposed control during load variations. Under this operating condition, the proposed controller controls the inverter to inject constant P and Q, to the grid side, corresponding to the desired powers, as illustrated in Figure 21a. In addition, it can be seen that the P_g and Q_g of the grid side decrease when the load is connected. This means that the load consumes a part of the injected power, and the rest goes to the main grid. According to Figure 21b, it can be observed that f_{VSI} and E_{VSI} remain unchanged, as well as the inverter sinusoidal current and voltage, v_{VSI}, and i_{VSI}, depicted in Figure 21c. Also, from Figure 21c, one can notice that the current of the grid decreases as the power decreases, and it has a pure sinusoidal waveform.

6 | PROCESSOR IN THE LOOP (PIL) IMPLEMENTATION

In this section, PIL simulation on PSIM environment is carried out to verify the proposed control algorithm. The built system is shown in Figure 22, where the system control is implemented on a DSP F28379D card that communicates with PSIM via a USB/JTAG link. In the PIL simulation, the PC is considered a virtual machine for emulating the grid-connected LC-filtered

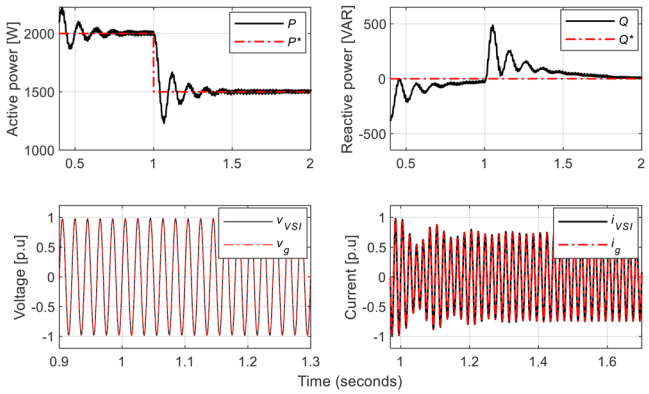

FIGURE 23 PIL results for P change, 2 to 1.5 kW, at $t = 1$ s

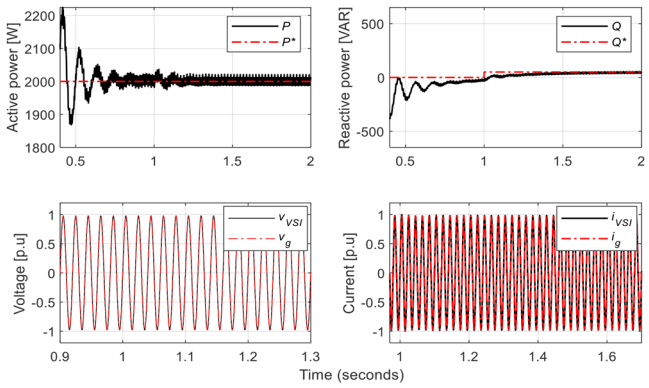

FIGURE 24 PIL results for Q change, 0 to 50 VAR, at $t = 1$ s

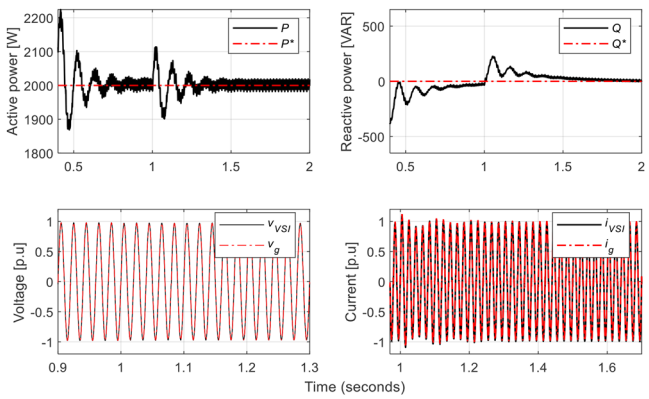

FIGURE 25 PIL results for *voltage* sag, 0.01 p. u, at $t = 1$ s

VSI system implemented in PSIM, while the control algorithm is running on a DSP μC [31, 32]. According to Figure 22, the filter current i_f, the inverter output voltage and current, v and i, and the grid voltage v_g are captured and provided to the DSP card as inputs, which in turn produces the duty cycle reference, D^*, to the PWM to generate the inverter switches' commands.

The same tests, as the previous ones in MATLAB simulations, are considered, which happen at $t = 1$ s. The obtained results are given in Figures 23 to 27, and they display the transient responses of the real and reactive power delivered by the

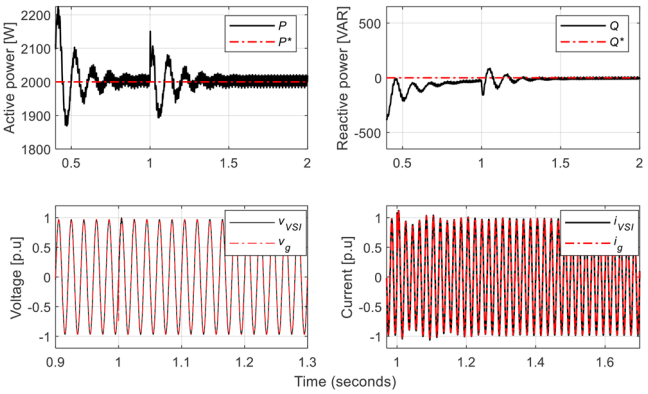

FIGURE 26 PIL results for phase jump with 50°, at $t = 1$ s

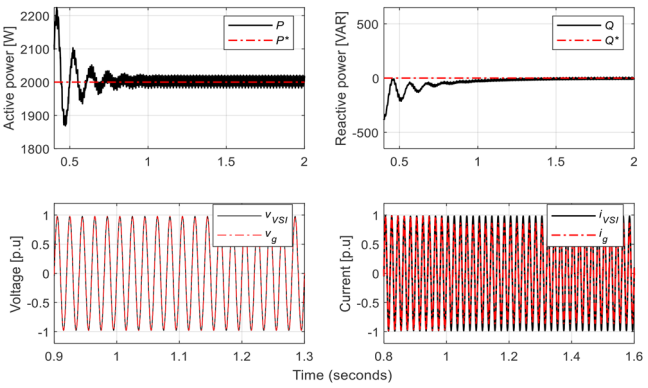

FIGURE 27 PIL results for load change ($R = 100\ \Omega$, L = 15 mH), at $t = 0.8$ s

inverter and their references as well as the voltage and current of the grid side and inverter side. The presented results show that the proposed controller can adjust the real and reactive power delivered by the inverter to their rated values. In addition, they demonstrate that the proposed controller can ensure the injection of proper sinusoidal current into the utility grid under different abnormalities.

7 | CONCLUSION

Advanced control scheme, dynamic phasor modelling, and analysis of the power control for a single-phase grid-connected droop-controlled VSI were developed in this paper. On one hand, a proposed control scheme that involves an ESOGI-based power calculation was adopted, to improve the power computation in terms of speed and accuracy, hence, the power control performance. On the other hand, a modelling approach based on the dynamic phasors taking into consideration the dynamics of the ESOGI-FLL-based power calculation was developed to derive the model of the power control-based grid-tied VSI. The small-signal model of the grid-tied VSI power flow as well as that describing the power computation dynamics based on the ESOGI-FLL were derived and their accuracy was verified. Then, the closed-loop small-signal model of the

overall system than power control was conducted. By using this model, the stability assessment is provided in order to determine the power controllers' gains. Simulation case studies based on a built grid-connected VSI system were conducted in the MATLAB/Simulink and PSIM's PIL frameworks. The obtained results corroborated the effectiveness and robustness of the designed power controller with regard to controlling the real and reactive power to the desired ones, meanwhile synchronizing with the main grid, under various grid disturbances. In addition, they reveal that a good transient response of power control with a settling time around 0.5 s and without oscillations is achieved. Practical implementation of the proposed control strategy will be the main focus in future work as well as developing grid support strategies to address stability issues arising from the integration of renewable energies to grid utility using power electronic interfaces.

ACKNOWLEDGEMENTS

The work of H. Ahmed is funded through the Sêr Cymru II 80761-BU-103 project by Welsh European Funding Office (WEFO) under the European Regional Development Fund (ERDF).

CONFLICT OF INTEREST

The authors declare that there is no conflict of interest.

DATA AVAILABILITY STATEMENT

The data that support the findings of this study are available from the corresponding author upon reasonable request.

ORCID

Abdelhammid Kherbachi https://orcid.org/0000-0002-6166-7744

REFERENCES

1. Bouzid A.M., et al.: A survey on control of electric power distributed generation systems for microgrid applications. Renew. Sustain. Energy Rev. 44, 751–766 (2015). https://doi.org/10.1016/j.rser.2015.01.016
2. Blaabjerg F., et al.: Distributed power-generation systems and protection. Proc. IEEE 105(7), 1311–1331 (2017). https://doi.org/10.1109/JPROC.2017.2696878
3. Hirsch A., Parag Y., Guerrero J.: Microgrids: A review of technologies, key drivers, and outstanding issues. Renew. Sustain. Energy Rev. 90, 402–411 (2018) https://doi.org/10.1016/j.rser.2018.03.040
4. Guerrero J.M., et al.: Hierarchical control of droop-controlled AC and DC microgrids—A general approach toward standardization. IEEE Trans. Industr. Electron. 58(1), 158–172 (2011). https://doi.org/10.1109/TIE.2010.2066534
5. Ahmed H., et al.: Robust gradient estimator for unknown frequency estimation in noisy environment: Application to grid-synchronization. IEEE Access 8, 70693–70702 (2020). https://doi.org/10.1109/ACCESS.2020.2986409
6. Akhavan A., et al.: Passivity enhancement of voltage-controlled inverters in grid-connected microgrids considering negative aspects of control delay and grid impedance variations. IEEE J. Emerg. Select Topics Power Electron. 9(6), 6637–6649 (2021). https://doi.org/10.1109/JESTPE.2021.3065671
7. Çelik D., Meral M.E.: A coordinated virtual impedance control scheme for three-phase four-leg inverters of electric vehicle to grid (V2G). Energy 246, 123354 (2022). https://doi.org/10.1016/j.energy.2022.123354
8. El Mariachet J., et al.: HIL-assessed fast and accurate single-phase power calculation algorithm for voltage source inverters supplying to high total demand distortion nonlinear loads. Electronics 9(10), 1643 (2020). https://doi.org/10.3390/electronics9101643
9. Yang Y., Blaabjerg F.: A new power calculation method for single-phase grid-connected systems. In: IEEE International Symposium on Industrial Electronics, pp. 1–6 (2013). https://doi.org/10.1109/ISIE.2013.6563684
10. Guerrero J.M., et al.: Decentralized control for parallel operation of distributed generation inverters using resistive output impedance. IEEE Trans.Industr. Electron. 54(2), 994–1004 (2007). https://doi.org/10.1109/TIE.2007.892621
11. Abusara M.A., Sharkh S.M., Guerrero J.M.: Improved droop control strategy for grid-connected inverters. Sustainable Energy Grids Networks 1, 10–19 (2015). doi.org/10.1016/j.segan.2014.10.002
12. Yang M., et al.: Small-signal stability analysis of the standalone single-phase parallel inverter with BPF-based droop control scheme. Paper presented at SPEC 4th Southern power electronics conference (IEEE), pp. 1–8 (2018). https://doi.org/10.1109/SPEC.2018.8636035
13. Kherbachi A., et al .: ARM-based implementation of SOGI-FLL method for power calculation in single-phase power system. Paper presented at ICEE 5th international conference on electrical engineering (IEEE), pp. 1–6 (2017). https://doi.org/10.1109/ICEE-B.2017.8192134
14. Kanavaros D., Oriti G., Julian A.L.: Implementation and comparison of active and reactive power flow control methods in a single-phase grid-connected microgrid. Paper presented at ECCE IEEE energy conversion congress and exposition, pp. 2800–2807 (2019). https://doi.org/10.1109/ECCE.2019.8913043
15. Leal A.d.J.C., Rodríguez T., Santamaria F.: Comparative of power calculation methods for single-phase systems under sinusoidal and non-sinusoidal operation. Energies 13 (2020), doi.org/10.3390/en13174322
16. Azevedo G.M.S., et al .: Enhanced power calculator for droop control in single-phase systems. Paper presented at IEEE Energy Conversion Congress and Exposition, pp. 391–396 (2011). https://doi.org/10.1109/ECCE.2011.6063796
17. Kherbachi A., et al .: Enhanced structure of second-order generalized integrator frequency-locked loop suitable for DC-offset rejection in single-phase systems. Electr. Power Syst. Res. 170, 348–357 (2019). https://doi.org/10.1016/j.epsr.2019.01.029
18. Coelho E.A.A., Cortizo P.C., Garcia P.F.D.: Small-signal stability for single-phase inverter connected to stiff AC system. Paper presented at conference record of the 1999 IEEE industry applications conference. Thirty-Forth IAS Annual Meeting (Cat. No.99CH36370), vol. 4, pp. 2180–2187 (1999). https://doi.org/10.1109/IAS.1999.798756
19. Guerrero J.M., et al .: Control strategy for flexible microgrid based on parallel line-interactive UPS Systems. IEEE Trans. Ind. Electron. 56(3), 726–736 (2009). https://doi.org/10.1109/TIE.2008.2009274
20. Pan D., et al.: Transient stability of voltage-source converters with grid-forming control: A design-oriented study. IEEE J. Emerg. Select. Topics Power Electron. 8(2), 1019–1033 (2020). https://doi.org/10.1109/JESTPE.2019.2946310
21. Yajuan G., et al.: An improved droop controller for grid-connected voltage source inverter in microgrid. In: 2nd International Symposium on Power Electronics for Distributed Generation Systems, pp. 823–828 (2010). https://doi.org/10.1109/PEDG.2010.5545801
22. Deng Y., et al.: Enhanced power flow control for grid-connected droop-controlled inverters with improved stability. IEEE Trans. Industr. Electron. 64(7), 5919–5929 (2017). https://doi.org/10.1109/TIE.2016.2606081
23. Verma V., Khushalani-Solanki S., Solanki J.: Modeling and criterion for voltage stability of grid-connected droop controlled inverter. In: North American Power Symposium (NAPS), pp. 1–5 (2017). https://doi.org/10.1109/NAPS.2017.8107346
24. Avelar H.J., et al.: A state equation model of a single-phase grid-connected inverter using a droop control scheme with extra phase shift control action. IEEE Trans. Industr. Electron. 59(3), 1527–1537 (2012). https://doi.org/10.1109/TIE.2011.2163372
25. Guo X., et al.: Dynamic phasors-based modeling and stability analysis of droop-controlled inverters for microgrid applications. IEEE Trans. Smart Grid 5(6), 2980–2987 (2014). https://doi.org/10.1109/TSG.2014.2331280

26. Díaz S.A., et al.: Comparison of modeling methodologies for inverters in grid-connected mode, controlled by droop scheme. Int. J. Appl. Eng. Res. 13(19), 14241–14253 (2018)
27. O'Rourke C.J., et al.: A geometric interpretation of reference frames and transformations: Dq0, Clarke, and Park. IEEE Trans. Energy Conver. 34(4), 2070–2083 (2019). https://doi.org/10.1109/TEC.2019.2941175
28. Alsaleh I., Fan L.: DQ-axis current-based droop controller. Paper presented at NAPS North American power symposium, pp. 1–6 (2017). https://doi.org/10.1109/NAPS.2017.8107382
29. Bendib A., et al.: New modeling approach of secondary control layer for autonomous single-phase microgrids. J. Franklin Inst. 356 (2019). https://doi.org/10.1016/j.jfranklin.2019.04.020
30. El Mariachet J., et al.: Power calculation algorithm for single-phase droop-operated inverters considering nonlinear loads and using n-order SOGI filtering. Paper presented at international conference on renewable energies and power quality, "Renewable Energy and Power Quality Journal (RE&PQJ)," pp. 710–715 (2018). DOI: 10.24084/repqj16.442
31. https://powersimtech.com/products/psim/psim-modules/processor-in-the-loop/
32. Ahmed H., Çelik D.: Sliding mode based adaptive linear neuron proportional resonant control of Vienna rectifier for performance improvement of electric vehicle charging system. J. Power Sources 542, 231788 (2022). https://doi.org/10.1016/j.jpowsour.2022.231788

How to cite this article: Bendib, A., Kherbachi, A., Chouder, A., Ahmed, H., Kara, K.: Advanced control scheme and dynamic phasor modelling of grid-tied droop-controlled inverters. IET Renew. Power Gener. 19, 1–19 (2025). https://doi.org/10.1049/rpg2.12610